Thunder Bay, Ontario, Canada

Wind Load Evaluation on Photovoltaic Modules with Flow Deflector

A thesis in partial fulfillment of

the requirements for the degree of

MASTER OF SCIENCE

in

MECHANICAL ENGINEERING

By

Naifu Xu

2020, September

ACKNOWLEDGMENTS

Gratefully appreciate my supervisor Dr. Ali Tarokh bare all my problems and patiently guide me through these years. The determination of being an honest engineer with a clear goal can never be done without the guidance of my supervisor.

Also, I'd like to appreciate the support of my family, who was there for me to go through those darkest times and make me who I am today.

The difficulty for me as a first-time abroad student that facing this amount of challenges can never be accomplished without the help and support from my supervisor, my family, and friends.

Also, I want to sincerely appreciate the time and efforts that my supervisor Dr. Ali Tarokh, and committee members Dr. Basel Ismail and Dr. Leila Pakzad, took on my thesis.

Again, thanks to everyone I met during this wonderful journey.

ABSTRACT OF THE THESIS

Wind Load Evaluation on Photovoltaic Modules with Flow Deflector

The wind load on a photovoltaic system and the effects of adding a flow deflector around the panel are studied. The deflector is a reinforce measurement aiming to reduce the aerodynamic wind loads over the PV system, which can lower the collapsing risk when the system is under extreme weather conditions. Simulations of wind flow over both stand-alone and arrayed PV modules are performed by using the SST $k-\omega$ turbulence model based on the Reynolds-Averaged Navier-Stokes equations. The inlet velocity profile is specified to describe the conditions representing the flows over a PV system located on a large open terrain with the atmospheric boundary layer. The calculations are compared to the data from the published wind flow simulations of the drag and lift force coefficients along the centerline of the module, and to the net pressure coefficient on the PV module. Further, the wind load over the PV system are compared for both stand-alone PV module and arrayed PV system with and without a flow deflector placed around it. The effects of the wind directions, the PV module inclination angles, the shapes of the deflector, and the spacings between the deflector and the module are investigated. The results show that when the inclination angle of the PV module is fixed to 25°, placing the deflector around the stand-alone module can generate a wind load reduction of up to 40%. For an arrayed PV system, the wind load is reduced by 8% on the first-row modules under the wind direction of 0°. Thus, the deflector offers an economical solution for reducing the wind load on the existing PV projects without modifying the modules or installation arrangements.

CONTENTS

Chapter 1. INTRODUCTION 1

1.1 Current Energy Structures 1

1.2 Brief introduction of the history of PV technology 2

1.3 Background and Introduction to The Current Study 3

Chapter 2. LITERATURE REVIEW 7

2.1 Wind Load Evaluations on Ground-mounted PV systems 7

2.2 Wind Load Evaluations on Roof-mounted PV Systems 11

2.3 Other research related to PV module 15

2.4 Summary 17

Chapter 3. PROBLEM DESCRIPTION AND METHODOLOGY 19

3.1 Problem Description 19

3.2 Turbulence Modeling 21

3.2.1 Reynolds-Averaged Navier-Stokes equations 21

3.2.2 Turbulence Model SST $\boldsymbol{k-\omega}$ 23

3.3 Computational Model 28

3.3.1 PV module and Additional Components Geometry Description 28

3.3.2 Computational Domain 31

3.3.3 Boundary Conditions 33

3.3.4 Computational Mesh Result and Simulating Time 34

Chapter 4. RESULTS AND DISCUSSION 37

4.1 Numerical Model Validations 39

4.1.1 Turbulence Model 39

4.1.2 Aerodynamic loading (Benchmark solution) 40

4.2 Flow Deflector Placed In Front of the PV Module 42

4.3 Flow Deflector Placed Around the PV Module 67

4.4 Different Spacing L_G 69

4.5 Different Module Inclination Angle θ 70

4.6 Wind Load Changes Applying the Deflector to the Arrayed Photovoltaic System 75

Chapter 5. CONCLUSIONS AND FUTURE WORKS 79
5.1 Conclusions 79
5.2 Future Works 80
APPENDIX A: Equations and Methodology 82
APPENDIX B: OpenFOAM Modifications 83
REFERENCE 84

LIST OF TABLES

Table 2. 1 Representative wind load research on ground-mounted cases 8

Table 2. 2 Representative wind load research on roof-mounted cases 12

Table 3. 1 Thesis problem description summary 21

Table 3. 2 SST $k-\omega$ turbulence model constants used in the current study 26

Table 3. 3 Distance of the PV module (coordinate origin) to the boundaries 31

Table 3. 4 Computational mesh independency test results at cell number between 0.8 to 2.2 million 35

Table 4. 1 Comparison of C_N on the module obtained from different turbulence models at wind direction of 45° 40

Table 4. 2 Surface pressure and C_N on the module under wind direction 0° with and without the flow deflector in front of the module 52

Table 4. 3 Surface pressure and C_N on the module under wind direction 45° with and without the flow deflector in front of the module 56

Table 4. 4 C_N on the module under wind direction 135° with and without the flow deflector in front of the module 59

Table 4. 5 Surface pressure and C_N on the module under wind direction 180° with and without the flow deflector in front of the module 63

Table 4. 6 C_N comparison with and without the deflector in front of the PV module 64

Table 4. 7 C_N comparison with and without the deflector placed around the PV module 68

Table 4. 9 C_N, C_L, and C_D over the module with deflector in front under wind direction 0° with different spacing L_G 70

Table 4. 8 C_N on the tested inclined module under wind direction 0° with and without the flow deflector in front of the module 73

LIST OF FIGURES

Figure 3. 1 Schematic diagram of the problem with the coordinate system (cross-section) 20

Figure 3. 3 Model geometry of simulation isolated PV module (a) front view, (b) side view 29

Figure 3. 4 Schematic diagrams of the geometry of the deflector and the placement: (a) front view of the deflector, (b) side view of the deflector, (c) schematic diagram of the placement of the deflector in the PV system 30

Figure 3. 5 Computational system domain schematic diagram 32

Figure 3. 6 Computational domain boundaries and axis descriptions 33

Figure 3. 7 Dimensionless inlet velocity profile 34

Figure 3. 8 (a) grids in multiple levels around the module and deflector, and (b) middle cross-section of the mesh 36

Figure 4. 1 Vertical position on the centerline of the domain ($y=0$) 38

Figure 4. 2 Velocity profile (left), TKE profile (right) comparison with different turbulence model [45] 39

Figure 4. 3 (a) A schematic view of the wind flow directions over the stand-alone PV module, (b) C_N, C_L, and C_D on the module comparison between the current study and Ref. [5] 41

Figure 4. 4 A schematic view of wind flow directions over the deflector-module combination 42

Figure 4. 5 3D velocity distribution view of the cross-sections of the centerline of the domain (*y=0*) and the reference height (*h = 0.6 m*) for wind direction 0° with the deflector-module combination structure 43
Figure 4. 6 Streamwise velocity distribution (a) without deflector and (b) with deflector under wind direction 0° 44
Figure 4. 7 Pressure coefficient distribution over mid-section of the windward surface of the module with and without the deflector (top), the definition of the wind direction and the surfaces (bottom left), and the schematic view of the midline, where *b* is the distance from the leading edge along with the breadth of the panel (bottom right) at wind direction of 0° 45
Figure 4. 8 (a) Streamwise velocity distribution and (b) TKE profile near the stand-alone PV module without the deflector under wind direction 0° at *X* = -0.6, -0.2, 0, 0.2, 0.6, 147
Figure 4. 9 (a) Streamwise velocity distribution and (b) TKE distribution for a PV module with a flow deflector in the front under wind direction 0° at *X* = -0.6, -0.2, 0, 0.2, 0.6, 1 49
Figure 4. 10 Flow streamlines near the PV module (a) without and (b) with the flow deflector under wind direction 0° 51
Figure 4. 11 Velocity distribution in the *x*-direction for a PV module under wind direction 45° (a) without the deflector and (b) with the deflector 53
Figure 4. 12 TKE distribution for a PV module under wind direction 45° (a) without the deflector and (b) with the deflector 55
Figure 4. 13 Velocity distribution in the *x*-direction for a PV module under wind direction 135° (a) without the deflector and (b) with the deflector 57

Figure 4. 14 TKE distribution near the PV module at $y = 0$ under wind direction 135° (a) without the deflector and (b) with the deflector..... 58
Figure 4. 15 Streamwise velocity distribution near a PV module at $y = 0$ under wind direction 180° (a) without the deflector and (b) with the deflector 60
Figure 4. 16 TKE distribution near a PV module under wind direction 180° (a) without the deflector and (b) with the deflector..... 62
Figure 4. 17 The C_N on the PV module before and after adding the flow deflector in front of the module 63
Figure 4. 18 (a) C_L and (b) C_D with and without the deflector in front of the stand-alone PV module 65
Figure 4. 19 A schematic view of wind flow directions over the deflector-module combination..... 67
Figure 4. 20 Comparison of the C_N on the PV module with and without the deflector placed around the module 68
Figure 4. 21 Comparison of the C_N on the PV system with different inclination angles.. 71
Figure 4. 22 Streamwise velocity distribution near a PV module at the inclination angle of 35° under wind direction 0° (a) without the deflector and (b) with the deflector 72
Figure 4. 23 Streamwise velocity distribution near arrayed panels (a) without and (b) with the flow deflector under wind direction 0° 75
Figure 4. 24 TKE distribution of arrayed panels (a) without and (b) with the deflector at wind direction 0°..... 76
Figure 4. 25 C_N of the module in each row of the array with and without the flow deflector in front 77

LIST OF ABBREVIATION AND SYMBOLS

Abbreviation	**Definition**
3D	Three dimensional
CFD	Computational fluid dynamics
FVM	Finite volume method
MW	Megawatt
NS	Navier Stokes
PV	Photovoltaic
RANS	Reynolds-Averaged Navier-Stokes
SST	Shear stress transport

Symbols	**Definition**
θ	Inclination angle
ρ	Density (air)
v	Kinematic viscosity
b	Distance from the leading edge of the module
C_N	Net pressure coefficient
C_L	Lift coefficient
C_D	Drag coefficient
W	Width of the computational domain
W_M	Width of the PV module
L	Length of the computational domain
L_M	Length of the PV module
L_D	Length of the flow deflector
H	Height of the computational domain
H_M	Height of the PV module
H_D	Height of the flow deflector
H_{ref}	Reference height (0.6 m)
U_0	Reference velocity (26 m/s)
U_{ref}	Velocity at reference height, 12 m/s

Chapter 1. INTRODUCTION

1.1 Current Energy Structures

As the most widely used form of energy, electricity is generated by converting primary sources of energy, such as coal, gasoline, nuclear, and solar. The current energy structure is the cause of two main concerns. First, the estimated time before the world runs out of fossil fuels is between 50 and 100 years; yet the world still relies highly on non-renewable primary resources. Second, the gas emissions from the fossil fuel combustion process have long had a severe influence on the global environment, with such outcomes as greenhouse effects, smog, and acid rain. According to *The World Bank*, the worldwide proportion of total primary energy sources attributable to fossil fuel consumption dropped from 94.1% in 1960 to 79.7% in 2015 [1]. However, the absolute consumption of fossil fuels is still climbing. Under such critical circumstances, the need for a transition to a sustainable society is widely recognized.

Solar energy is one of the cleanest alternatives to fossil fuels. The photovoltaic (PV) system can convert solar energy directly into electricity. Freed electrons generate the electric current when the sunlight reaches the semiconductor in the PV cell [2]. Therefore, no gas emissions are produced in the use of PV systems. Moreover, the general unit of the

use of PV technology is a PV module, which contains some connected and framed PV cells. The modules can be later wired and scaled to meet the various power demands. In Canada, one of the leading countries in utilizing different types of renewable energy, 17% of the required energy was provided from renewable sources in 2018. However, only 0.6% of that comprised PV systems, most of which were from the province of Ontario. The installed capacity rose from 500 *MW* in 2010 to 3040 *MW* in 2018, and it is still growing [3]. In addition, the price of the PV modules dropped from 8.08 Canadian dollars/watt in 2004 to 0.99 Canadian dollars/watt in 2018. Trends indicate that operating expenses keep dropping, and predictions put the price below 0.9 Canadian dollars/watt by 2022 [4]. The advantages of a clean and cheap power supply with significant potential means that the beginning of the new decade will see a massive market for PV systems in countries with lots of available land resources, including Canada.

1.2 Brief introduction of the history of PV technology

The history of PV systems started in 1839 when the PV effect was first discovered by Edmond Becquerel. It was not until 1905 when the photon was first explained that Einstein proposed a theory of the law of the PV effect. The first functional selenium PV cell was invented by Charles Fritts in 1883 and was later be used to build the world's first roof-

mounted PV system [4]. However, the low efficiency (1%) and very high cost (it used a thin layer of gold) prevented widespread acceptance by the public. PV systems' current efficiency of roughly 22% and reduced capital costs mean that PV systems are attracting and being accepted by more consumers.

1.3 Background and Introduction to The Current Study

Although the main cost of a PV system arises from the PV modules, the cost of the holding structure can be considerable. Therefore, wind estimates must be used when support structures are designed to ensure that systems have enough wind load resistance to prevent them from collapsing in extreme weather conditions. Support structures for PV systems are designed in accordance with the characteristics of the location of the installation, such as wind profile, surrounding structures, etc., which makes it difficult to estimate the wind load by following general national engineering codes (such as the codes provided by the American Society of Civil Engineers, the National Building Code of Canada, etc.). The overestimated wind load leads to the over-cost of the initial investment, while there is a higher risk of the system collapsing if the wind load is underestimated.

Wind load is a significant factor while designing the support structures. In order to meet the wind resistance requirements and to avoid the system mechanism failure under extreme

weather conditions, support structures take a considerable fraction of the total system capital cost. Therefore, designs are proposed to reduce the wind load by either making modifications on the PV module or using additional structures to block the majority of the wind flow. However, changing the geometry of the module can be expensive and sometimes impossible to be adopted by the existing PV projects. Take a single PV module as an example, which the current price for a typical 100W/12V module is around 120 Canadian dollars. From the user point of view, to achieve the wind load reduction on such a module by replacing it with a module with modified geometry (such as hollow), the minimum cost will be the price for a new module, which is $120. From the manufacturing point of view, opening new assembly lines for PV modules with new geometry is risky and may cost up to thousands. Also, a certain amount of wind flow can help naturally maintain the temperature of the module in functional criteria without using the cooling systems.

Thus, to reduce the wind load without changing the geometry of the PV modules and maintain the natural air-cooling ability, the effect of adding a flow deflector to a PV system is investigated in the current study. The geometry of the deflector is designed to be simple, which is a tilted flat plate with low height placing from a certain distance around the PV module. The purpose is to use the deflector to deviate the flow, changing the vortex structure at the leeward side of the PV module to reduce the wind load. Because of the

geometry simplicity, the material of the deflector can be selected at a negligible cost. For instance, the deflector can be made using the construction leftovers with similar geometry, which minimizes the cost for both users and manufacturers. The wind load reduction after adding the deflector reaches a maximum of 39 percent, as shown in the simulations.

The current study evaluates the effects after applying the flow deflector to a PV system. Five chapters are divided. Chapter 2 goes through the existing research, mainly categorized by the mounting locations of the PV systems. Chapter 3 addresses the problem to be solved in the current study and the methodologies. Chapter 4 presents the results and discussions. Finally, conclusions and ideas for future work are discussed in Chapter 5.

The research objectives are:

I. Validate the results from reference research [5]

II. Evaluate wind loads on a stand-alone PV module at different wind directions, with and without a flow deflector

III. Investigate wind loads on a PV module with and without the flow deflector, at different PV module inclination angles

IV. Evaluate the effects of spacing between the deflector and the PV module at a wind direction of 0°

V. Investigate wind loads on a five-row PV array with and without a flow deflector, at a wind direction of 0°

Chapter 2. LITERATURE REVIEW

The experimental measurements and numerical simulations have been utilized by researchers to evaluate the wind load on PV systems under different configurations. Categorized by the mounting locations, the studies can be divided into ground-mounted and roof-mounted cases. Additional PV module-related studies are included and discussed.

2.1 Wind Load Evaluations on Ground-mounted PV systems

Table 2.1 contains some of the representative studies on evaluating the wind load on ground-mounted PV systems.

The ground-mounted PV farm is a commonly used PV system form. The PV farm contributes to the majority of the on-grid electricity produced by PV applications. Therefore, experiments and numerical simulations on wind load evaluations can help create a better design for the PV projects.

Table 2. 1 Representative wind load research on ground-mounted cases

Reference	Tested configuration(s)	Method
Jubayer et al. [5][6]	wind directions: 0°, 45°, 135°, 180°	CFD
BAETU et al. [7]	wind directions: 0°, 30°, 45°, 135°, 180°	CFD
Shademan et al. [8]	ground clearance (*H/L*): 0.22, 0.66, 1.11	CFD
Warsido et al. [9]	row spacing, column spacing in an array	experiment
Ayodeji et al. [10]	wind directions, the inclination angle	experiment
Reina et al. [11]	wind directions, the inclination angle	CFD
Mammar et al. [12]	ground clearance: 0.53, 0.84, 1.15	experiment
Irtaza et al. [13]	wind directions, the inclination angle	CFD

Ayodeji et al. [10] evaluated the wind direction effects on wind load on PV systems experimentally. The study focused on two different wind directions (30°, 150°), where the PV modules are found experiencing higher pressure at the close wind direction edge regions. A similar conclusion can be found by the experiments performed by Lopez et al. [14], where the largest value of pressure coefficient is located at a small area close to the edge of the module. Additionally, the maximum pressure coefficient values can be found for wind directions of 45° and 135°, which should be carefully considered for the PV

project for possible local damages. With the rapid development of computational capabilities, numerical simulations are adapted and performed as an alternative research method, including the field study of wind load evaluation on PV systems. Georgeta et al. [7] conducted the numerical simulations evaluating wind direction effects on wind load over the PV system. The flow structure around the PV module is virtualized, where a low-velocity region can be found at the leeward side of the module. This low-velocity conical vortices region generates the largest suction at wind direction 45° when the inclination angle of the module is 30°. The agreement can be found with the experiment by Lopez et al. [14], which explained that the wind load on the module at wind direction 45° is critical because the largest suction leads to the largest pressure difference between both sides of the module. Shademan et al. [8] evaluated wind load on a stand-alone PV module without the support structure and found that the panel experiences the maximum aerodynamic wind load at wind directions of 0° and 180°. Also, the bottom half of the panel experiences the most significant pressure difference, which indicates that this region is vulnerable and needs special consideration during the design process.

The spacing gap size between rows and columns in a PV matrix is another critical factor that affects the wind load over the PV system. Warsido et al. [9] performed experiments to investigate the effect of column and row spacing size on wind load. The results showed

that the wind load on a stand-alone module is higher than in an array. Also, the wind load on the outer ring of the array is higher than in the inner sections. The effect of column spacing on wind load is minimal, while wind load increases with the rise of row spacing. The inner panel gap effect on wind load was investigated by Shademan et al. [8] through numerical simulations. It was found that small vortices are generated at the leeward side close to the gaps, and the strength of the vortices increased with the rise of the gap size. A local drop of pressure on the module can be found with a slight increase in wind load around the gap area.

Ground clearance is the distance between the leading edge of the PV module and the ground, which is another configuration examined by Mammar et al. [12]. The results showed the same pattern with the numerical simulations by Shademan et al. [15], where the increased ground clearance leads to higher wind load. The rise of the vertical height of the module leads to a stronger vortex shedding with a natural form at the leeward side. Since the vortex enlarges the pressure difference between both sides of the module, the module should be installed close to the ground to avoid vortex shedding forms by the separation flow from the bottom edge of the module to develop a natural form.

Both Ayodeji et al. [10][16] and Reina et al. [11] investigated the inclination angle effect on the wind load on PV systems. An agreement can be found that within the inclination angle range from 25° to 40°, the wind load increases with the rise of the inclination angle.

2.2 Wind Load Evaluations on Roof-mounted PV Systems

Reviews of wind load evaluations on roof-mounted PV panels have been discussed previously by Stathopoulos et al. [17]. The first published study was back in 1986 [18]. Representative studies are categorized in Table 2.2.

Table 2. 2 Representative wind load research on roof-mounted cases

Reference	Tested configurations	Roof shape
Radu et al. [18]	wind directions, number of rows	flat
Ruscheweyh et al. [19]	roof heights, the inclination angle, row spacing	flat
Kopp et al. [20][21]	the inclination angle, roof heights, row spacing	flat
Browne et al. [22]	wind directions, building heights	flat
Aly et al. [23]	array arrangement	slope (3:12, 5:12)
Cao et al. [24]	the inclination angle, number of rows	flat
Pratt et al. [25]	the inclination angle, panel location	flat
Banks [26]	building geometry, wind directions	flat
Geurts et al. [27]	wind directions, model scale	slope
Stenabaugh et al. [28]	inner-panel gap size	slope (7:12)
Naeiji et al. [29]	roof shape	flat, gable, hip
Wang et al. [30]	side ratio, aspect ratio, parapet height	flat
Chu et al. [31]	wind directions, parapet height	flat with parapet

Wind direction plays an important role in influencing the wind load over roof-mounted PV systems. Similar to the effect on the ground-mounted PV systems, experiments were conducted to investigate the wind load on a PV system on a flat roof by Ruscheweth et al. [19]. Wind directions from 0° to 60° were tested with a uniformed module inclination angle

of 30°, which shows that the outer ring of the PV array is experiencing the most significant wind load. The sheltering effect caused by the edge of the roof and the rim of the PV field leads to a wind load reduction in the inner PV array field. Browne et al. [22] brought the parapet effect of the building into consideration. The peak loading pattern was found different from the bare roof, suggesting that the design of the PV arrays mounted on the roof should be cautious with the existence of the parapet since the averaged peak wind load on the PV array is increased with the parapet height in the range of 1 to 7 times of the height of the module [22]. The experiment results produced by Chu et al. [31] show that the panel experiences maximum wind load at wind direction 45° with an inclination angle of 45°. This is showing an agreement with ground-mounted cases [14]. Moreover, projects were performed to compare the experimental results with values provided by designing guidelines. A considerable overestimation of the wind load on residential roof-mounted PV systems was found both by Geurts et al. [27] and Ortiz et al. [32] with different PV module geometry.

The roof has limited space, which higher the requirement of the system installation arrangements [18]. Aly et al. [23] carried out wind tunnel projects to evaluate the placement of the PV module on a residential gable roof. The net pressure distribution on the gable roof showed significantly different results compared with those mounted on a flat roof. The

installation of the PV modules on such gable roofs should avoid the corners, edges, and ridges. The number of rows of PV modules in an array is investigated by Cao et al. [24]. The experimental results show that the multi-array PV system is experiencing a lower external force than on the flat roof, which is unfavorable to the PV system. Also, with increasing the row-spacing, the panel-generated turbulence is enhanced, which leads to a higher external force that should be avoided. The turbulence changes in increasing the inclination angle of the PV module is analyzed by Pratt et al. [25]. The same flow pattern can be found within the ground-mounted studies [10][11].

The building geometry is an essential factor that affects the wind load distribution on the roof. Kopp et al. [21] carried out the experiments following the engineering guidelines to evaluate wind load under different zones on the PV system mounted on the flat roof. The building height is affecting the wind load at the roof-edge zones, where the wind load tends to be higher than other zones. The high wind load area for a low-rise building is found, reaching up to 40% of the mean roof height from the roof edge to the inner area. Larger building height can extend this high wind load area. Therefore, the experiments performed by Banks [26] showed that the corner high wind load zones are more critical for the PV system than the edge generated ones, in which the PV systems are suggested to be

positioned higher than two building-level heights from the roof edges. The agreements can be found within other experiments with different building geometries [29], [30].

2.3 Other research related to PV module

Since the computational simulations are restricted by the available computational resources, a possible solution for limited calculating resources was proposed by Reina et al. [11]. The periodic model can generate acceptable results compared to full three-dimensional models. With further validations, this can be a practical alternative choice for general wind load evaluations on PV projects. The project by Schellenberg et al. [33] used nonlinear response-history analysis to evaluate the design of the PV system structures, which get a better understanding of the mechanical response of the support structures under wind loads.

Scale issue is a newly categorized problem that should be carefully considered in future studies. Aly et al. [34] performed experiments and CFD simulations to compare the scale of the PV system from 1:1, 1:10, and 1:20 to 1:50. Both the mean pressure and the peak pressure under these scales showed agreement, which indicated that these scales were acceptable for investigations on wind load on ground-mounted PV systems. Based on the experiments by Aly et al. [35], instead of full-scale simulations, scales 1:20 and 1:30 are

preferred during scaled research. In general, local mean value and peak value drops can be obtained for scaled experiments or simulations compared with full-scale ones. Therefore, with the advantage of performing full-scale research numerically using computational tools, future simulations are suggested to proceed on a 1:1 scale.

Based on the studies mentioned in the previous sections, some simulations and experiments were performed to evaluate adding structures or modifying the PV module geometry to reduce the wind load.

Scaled experiments were performed by Chung et al. [36] to propose a design to reduce the wind load using a water tank-shaped particle. The research added a water tank-shaped particle above the panel. The uplift force was proven to be effectively reduced. Further studies were conducted later in 2010 with the same model [37] to verify the effect of using a guide plate at the top edge of the leeward side of the PV module with the water tank-shaped particle at the top of the module. The guide plate was found effective in reducing the negative pressure at the close leeward surface region of the module. Chung also proposed a similar idea in 2014 with only a guide plate at the back of the panel [38]. Similarly, in 2018, Ivo suggested adding a heat release plate to help the system cooling, which had the potential to reduce the negative pressure at the back of the surface [39]. Prost

et al. [40] experimented on reducing mean wind force over the photovoltaic system by using aerodynamic appendages, including hanging walls and eaves.

Markousi et al. [41] suggested a design that makes the PV module hollow. The simulation results showed that the wind load was effectively reduced by up to 12 percent. Another analysis was on the barrier effect analyzed by Bendjebbas et al. [42]. The airflow simulations showed that the barrier reduced wind velocity significantly while enhancing the stability of the panels within the reduction area.

2.4 Summary

The wind load reduction designs on the PV systems can be achieved by either modifying the geometry of the module or adding structures to the PV system. However, the former designs are expensive or even sometimes impossible to apply to the PV systems that already exist. The PV farms built in the suburban area can easily be affected by the expansion of the city, where solutions are needed to deal with the velocity increase in the PV field when buildings are built around the farm. Changing the geometry of each individual module on the farm is not an economical solution. The later designs can be summarized as using a barrier to block the airflow, significantly reducing the wind flow velocity in the PV field. However, the experiments by Schwingshackl et al. [43] showed

that the wind is relevant to the temperature of the PV module, where the temperature is directly related to the efficiency of the electricity generation. The dramatic amount of airflow reduction leads to the inhibition of the ability of natural cooling from the airflow.

Thus, the flow deflector is designed to not make any modification to the PV module and maintain the natural cooling ability from the airflow.

Chapter 3. PROBLEM DESCRIPTION AND METHODOLOGY

3.1 Problem Description

The wind load on a PV system with and without a flow deflector placed around the module is investigated in the current study. The shape change of the module is not considered in the current study, and the temperature in the domain is assumed to be constant at 15℃. Therefore, the density of the dry air at 101.325 kPa in the domain remains constant, with a value of 1.225 kg/m^3.

The two-dimensional schematic diagram of the cross-section of the problem with the coordinate system is shown in Figure 3.1. At wind direction 0°, the inclined PV module with the holding structure and the deflector is located close to the inlet with a distance of $9H_M$, in which the inlet flow can be fully developed.

The effect of wind directions on wind load is investigated from 0° to 180°. According to Jacobson et al. [44], the estimated optimal inclination angles of the PV system worldwide is within the range between 0° to 60°. Therefore, the inclination angles of the module are also investigated from 25° to 55° with a 10° interval. The spacing between the module and the deflector are tested by 0.5 W_M, W_M, 1.5 W_M separately, where the W_M is the width of the PV module. The geometry of the deflector is also altered by shape and height (0.3 m,

0.5 m, 0.7 m) and tested individually. Finally, the wind load on a 5-row PV system is evaluated with and without the flow deflector placing ahead of the first-row module.

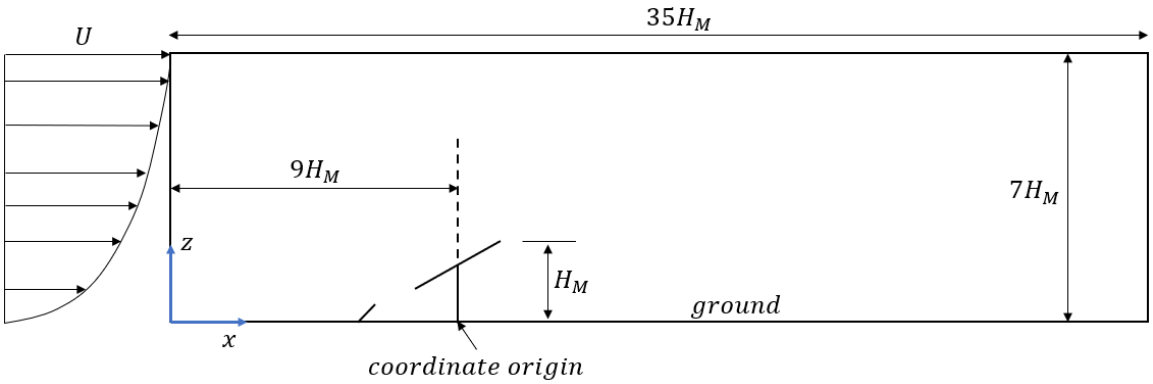

Figure 3. 1 Schematic diagram of the problem with the coordinate system (cross-section)

The aerodynamic boundary conditions are: an atmospheric boundary layer is employed at the inlet to simulate the open terrain wind flow. The outlet pressure is set to be zero gradients. No-slip condition is imposed on the ground and PV systems. The rest of the boundaries, including the top of the domain, is symmetry.

The problem description is summarized in Table 3.1.

Table 3. 1 Thesis problem description summary

Cases	Inclination angle (°)	Wind direction (°)	Spacing (W_M)
Stand-alone module	25 – 55	0 – 180	-
Module with deflector in front	25 – 55	0 – 180	0.5, 1, 1.5
Module with deflector around	25	0 – 180	0.5
Array	25	0	-
Array with deflector in front	25	0	0.5

3.2 Turbulence Modeling

3.2.1 Reynolds-Averaged Navier-Stokes equations

In the current study, the incompressible steady airflow can be described using the Navier-Stokes (NS) equations. Without the density variations nor heat transfer, the simplified form of NS equation is used, which is stated in Appendix A. The NS equations are nonhomogeneous, second-order, partial differential equations that have no analytical solution. Therefore, numerical techniques should be employed to solve them over the computational domain. Among the different numerical methods that are proposed for solving the NS equations, the Reynolds-averaged Navier-Stokes (RANS) method requires

fewer computational resources and can produce results faster. Although using a more accurate method, such as direct numerical simulation or large eddy simulation can provide more accurate results, the computational cost of using these models is very high since all the turbulence scales must be resolved in the computational mesh, which generally requires an approximate number of Re^3 mesh points (where Re is the turbulent Reynolds number) for one simulation [45]. The main objective of the current study is to evaluate the wind load on PV systems in the steady-state condition, for which the error of the turbulence modeling is negligible. Therefore, the focus of the study is the mean flow and the effects of turbulence on mean flow properties. Thus, the flow variables can be divided into the sum of the mean value (representing the mean flow) and the turbulence fluctuating component (representing the turbulence). The simplified RANS equations for the incompressible steady flow are listed as follows:

$$div\,\mathbf{U} = 0 \qquad (3-1)$$

$$div(U\mathbf{U}) = -\frac{1}{\rho}\frac{\partial P}{\partial x} + v\,div\big(grad(U)\big) + \frac{1}{\rho}\left[\frac{\partial(-\rho\overline{u'^2})}{\partial x} + \frac{\partial(-\rho\overline{u'v'})}{\partial y} + \frac{\partial(-\rho\overline{u'w'})}{\partial z}\right] \qquad (3-2a)$$

$$div(V\mathbf{U}) = -\frac{1}{\rho}\frac{\partial P}{\partial y} + v\,div\big(grad(V)\big) + \frac{1}{\rho}\left[\frac{\partial(-\rho\overline{u'v'})}{\partial x} + \frac{\partial(-\rho\overline{v'^2})}{\partial y} + \frac{\partial(-\rho\overline{v'w'})}{\partial z}\right] \qquad (3-2b)$$

$$div(W\mathbf{U}) = -\frac{1}{\rho}\frac{\partial P}{\partial y} + v\,div\big(grad(W)\big) + \frac{1}{\rho}\left[\frac{\partial(-\rho\overline{u'v'})}{\partial x} + \frac{\partial(-\rho\overline{v'^2})}{\partial y} + \frac{\partial(-\rho\overline{v'w'})}{\partial z}\right] \qquad (3-2c)$$

In the equations, *U, V, and W* are mean velocity components in *x, y, and z,* respectively. ρ is air density, *P* is pressure, *v* is kinematic viscosity, and $u', v', and\ w'$ are the turbulence fluctuation components. The term $\rho\overline{u'v'}$ here is called the "Reynolds stress" term. In order to be able to compute the turbulent flow with the RANS equations, turbulence models are needed to predict the Reynolds stress. The accuracy of commonly used RANS models is evaluated. The standard $k-\varepsilon$, RNG $k-\varepsilon$, and realizable $k-\varepsilon$ closures are used, along with the standard $k-\omega$, SST $k-\omega$, and RSM. Also referencing the turbulence model accuracy research by Tarokh et al. [46], and the benchmark study by Jubayer et al. [5], turbulence model SST $k-\omega$ is selected for the current study.

3.2.2 Turbulence Model SST $k-\omega$

The SST $k-\omega$ model is a two-equation blended turbulence model solved along with the RANS equations. In general, the model uses a function to control the model using either a $k-\varepsilon$ or $k-\omega$ turbulence model [47], since, from the field experience, $k-\varepsilon$ performs better at the off-wall region, and $k-\omega$ performs better close to the wall boundaries.

The simplified form of the $k-\varepsilon$ can be written as:

$$div(pk\mathbf{U}) = div\left[\frac{\mu_t}{\sigma_k} grad\ k\right] + 2\mu_t S_{ij}\cdot S_{ij} - \rho\varepsilon \qquad (3-3)$$

$$div(p\varepsilon\mathbf{U}) = div\left[\frac{\mu_t}{\sigma_\varepsilon} grad\ \varepsilon\right] + C_{1\varepsilon}\frac{\varepsilon}{k}2\mu_t S_{ij}\cdot S_{ij} - C_{2\varepsilon}\rho\frac{\varepsilon^2}{k} \qquad (3-4)$$

In equation (3-3) and (3-4), k is the turbulent kinetic energy, and ε is the dissipation of turbulent kinetic energy per mass, μ_t is the eddy viscosity, which is defined as:

$$\mu_t = C\rho\vartheta l = \rho C_\mu \frac{k^2}{\varepsilon} \qquad (3-5)$$

$$\vartheta = k^{1/2} \qquad (3-6)$$

$$l = \frac{k^{3/2}}{\varepsilon} \qquad (3-7)$$

C_μ is the dimensionless constant with a value of 0.09. The explanation of the terms in the equations of (3-3), (3-4) can be found in Appendix A.

The $k-\varepsilon$ turbulence model needs a wall function that relates the local wall shear stress to the mean velocity on the wall boundaries. Therefore, the mesh quality at the close wall regions is critical since it affects the accuracy of the prediction of the velocity fields in this region.

In order to avoid the misprediction caused by the mesh quality and wall functions, the $k-\omega$ model is proposed.

The turbulence frequency, $\omega = \varepsilon/k$, is introduced. The turbulence viscosity can be now written as:

$$\mu_t = \frac{\rho k}{\omega} \qquad (3-8)$$

The $k-\omega$ model can be written as:

$$div(\rho k\mathbf{U}) = div\left[\left(\mu + \frac{\mu_t}{\sigma_k}\right) grad(k)\right] + \left(2\mu_t S_{ij}\cdot S_{ij} - \frac{2}{3}\rho k\frac{\partial U_i}{\partial x_j}\beta_{ij}\right) - \beta^*\rho k\omega \qquad (3-9)$$

$$div(\rho\omega\mathbf{U}) = div\left[\left(\mu + \frac{\mu_t}{\sigma_\omega}\right) grad(\omega)\right] + \gamma_1\left(2\rho S_{ij}\cdot S_{ij} - \frac{2}{3}\rho\omega\frac{\partial U_i}{\partial x_j}\beta_{ij}\right) - \beta_1\rho\omega^2 \qquad (3-10)$$

In the equations (3-9), (3-10), the terms β^*, β_1 are constants whose value can be found in Table 3.1.

Compared with equation (3-4) in the $k-\varepsilon$ model and (3-10) in the $k-\omega$ model, the additional source term is found in the rate of production term. This gives a better sense of the turbulence kinematic value evaluation.

Thus, by using an engineering treatment to multiply the additional term by $(1-F_1)$, the blended model is controlled by using the blending function F_1, where

$$F1 = \tanh\left(arg_1^4\right) \qquad (3-11)$$

The arg_1 depends on the distance from the cell to the closest wall. And when $F_1 = 0$, the blended model works as $k-\varepsilon$, and $F_1 = 1$ indicates that the model works as $k-\omega$. In the SST model, the second function F_2 works as a viscosity limiter to achieve better agreement over the prediction of the separated flows with the experiments. The turbulence viscosity is transformed into

$$\mu_t = \frac{a_1 \rho k}{\max(a_1 \omega, SF_2)} \qquad (3-12)$$

Here, a_1 is a defined constant, and the S is the magnitude of the shear stress. The constants in the above functions are obtained from the research done by Mentor et al. [47].

Table 3. 2 SST $k-\omega$ turbulence model constants used in the current study

σ_k	$\sigma_{\omega,1}$	$\sigma_{\omega,2}$	γ_1	γ_2	β_1	β_2	β^*
1.0	2.0	1.17	0.553	0.44	0.075	0.083	0.09

The finite volume method is used to discretize the governing equations, and the SIMPLE (Semi-Implicit Method for Pressure Linked Equations) algorithm is employed to solve the discretized equations. The schematic view of the SIMPLE method is presented in Figure 3.2.

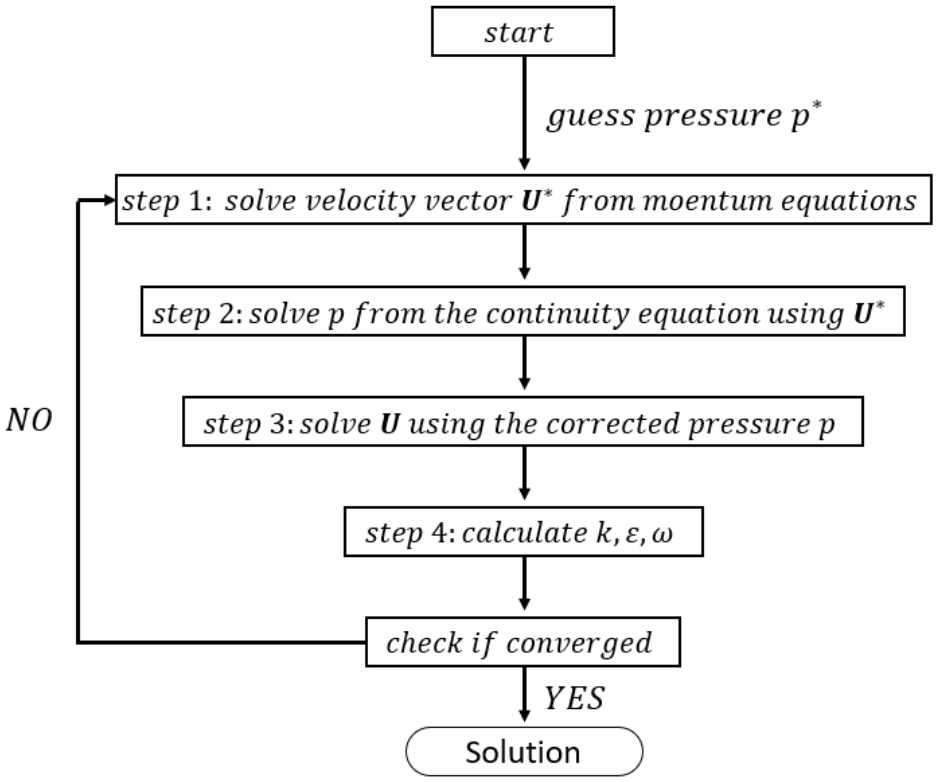

Figure 3.2 SIMPLE Algorithm flow chart

p^* is the guessed pressure value, $\boldsymbol{U}^*$ is the velocity vector calculated from the momentum equations using the guessed pressure value p^*, p is the corrected pressure calculated from the continuity equation using the velocity vector $\boldsymbol{U}^*$, and $\boldsymbol{U}$ is the corrected velocity vector using the corrected pressure p. k, ε, ω are kinetic energy, dissipation rate of the kinetic energy, and turbulence frequency, respectively.

3.3 Computational Model

The boundary conditions in the current study are set to simulate wind flow in an open terrain where the PV system is placed. The simulations are performed on a scale of 1:10. The descriptions of the dimensions in this section, including the geometry of the module, the flow deflector, and the computational domain, are stated in full-scale values.

3.3.1 PV module and Additional Components Geometry Description

The dimensions of the PV module for this study are selected from the geometry setup in Ref. [5].

The geometry of the PV module follows: 2.4 m in width (W_M), 7.2 m in length (L_M), and 1.7 m in height (H_M) with a thickness of 0.04 m according to commercial standard module thickness. The support pillars are cuboids, each with a width of 0.1 m. One pillar is located under the center of the module; the other two are symmetrically positioned in relation to the central pillar along the middle line of the module with a distance of 6 m. The inclination angle θ in the current study is verified within 25° to 55° with a 10° interval. The schematic diagram of the geometries is shown in Figure 3.3.

Distinct from the PV system in Ref [5], the structure that holds the PV module is considered in the current study.

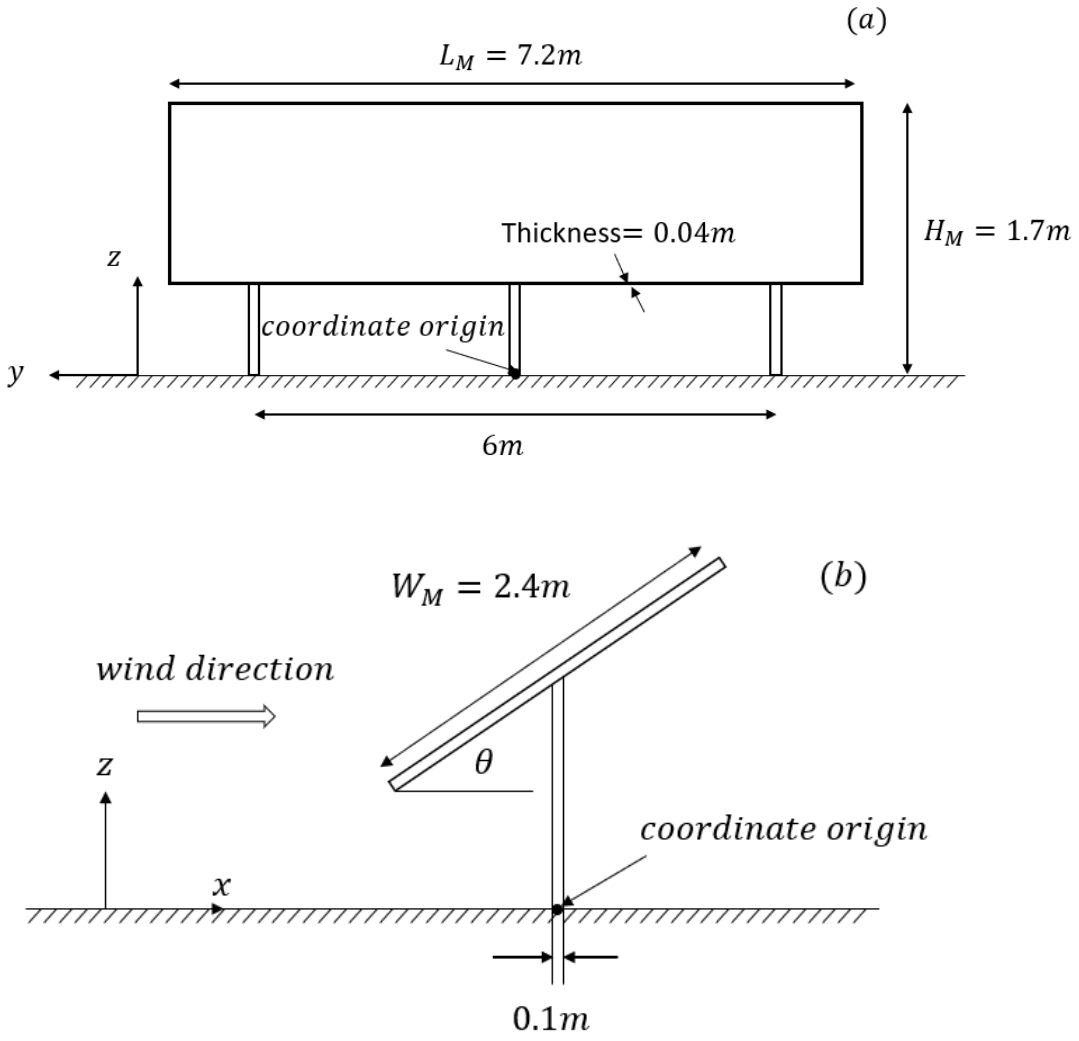

Figure 3. 2 Model geometry of simulation isolated PV module (a) front view, (b) side view

To cause the flow to deviate from the sides, the flow deflector is designed such that it is wider than the length of the PV module (7.2 m). The dimensions of the deflector follow: 8 m in length (L_D) and 0.5 m in height (H_D) with a uniform tilt angle of 45° and a thickness of 0.04 m, *as* shown in Figure 3.4. The deflector is placed with a gap size of L_G between

the closest edges of the deflector and the PV panel. Gap sizes of 0.5 W_M, W_M, and 1.5 W_M are tested, respectively.

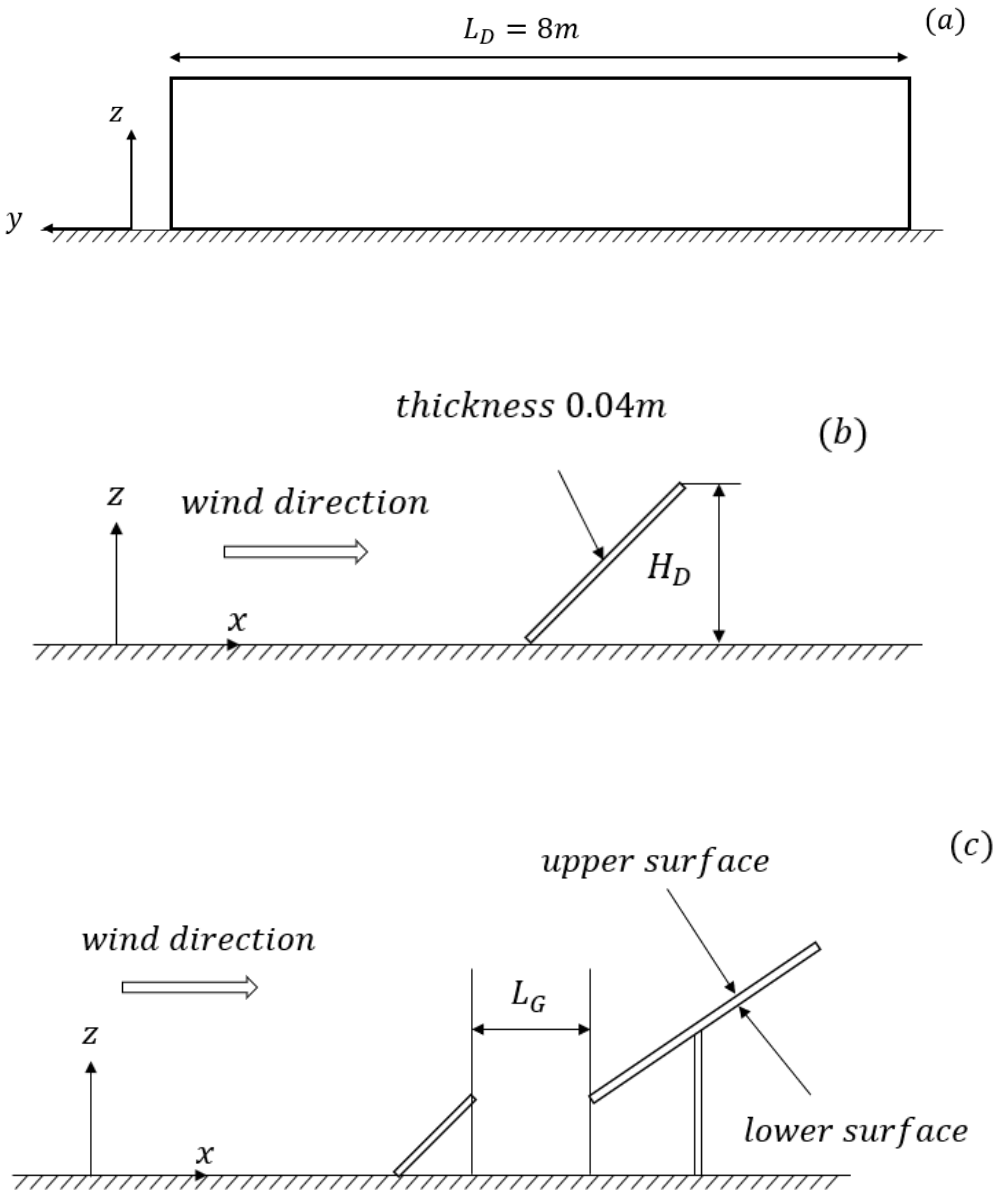

Figure 3. 3 Schematic diagrams of the geometry of the deflector and the placement: (a) front view of the deflector, (b) side view of the deflector, (c) schematic diagram of the placement of the deflector in the PV system

3.3.2 Computational Domain

The dimensions of the computational domain can be defined using the characteristic values, which are $36H_M$ in length (L), $24H_M$ in width (W), and $6H_M$ in height (H). The placement of the PV module in the computational domain is defined in Table 3.2. The overall domain schematic diagram can be found in Figure 3.5.

Table 3. 3 Distance of the PV module (coordinate origin) to the boundaries

Boundary	characteristic value	actual value
inlet	$9H_M$	$15m$
outlet	$27H_M$	$45m$
front	$12H_M$	$20m$
back	$12H_M$	$20m$
top	$6H_M$	$10m$

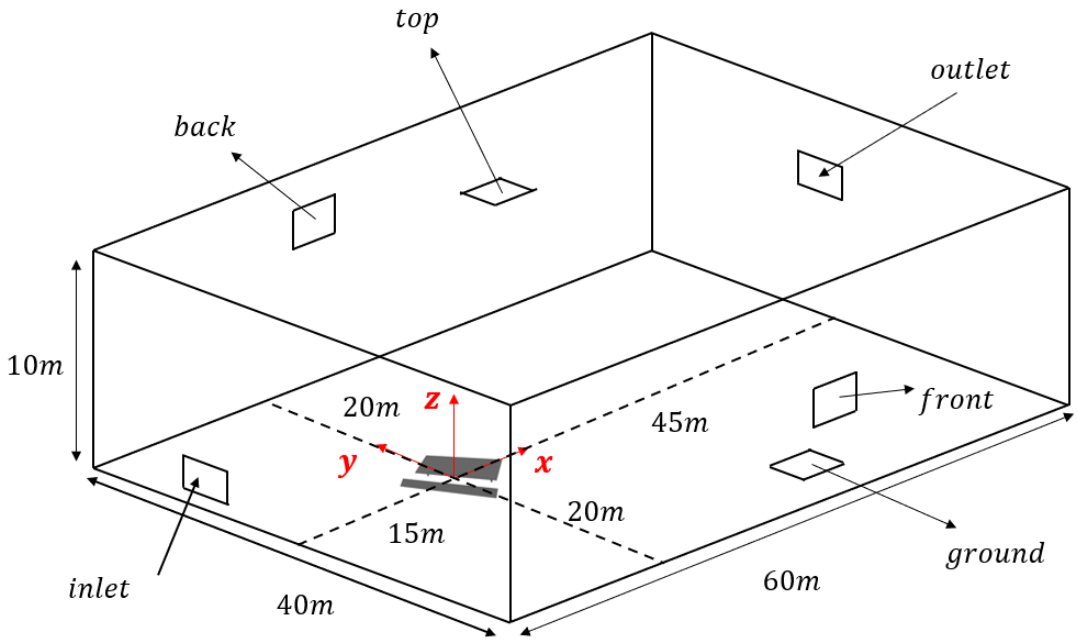

Figure 3. 4 Computational system domain schematic diagram

The description of the coordinate origin can be found in section 3.3.1.

3.3.3 Boundary Conditions

The schematic diagram of the definition of the boundaries is introduced in Figure 3.6.

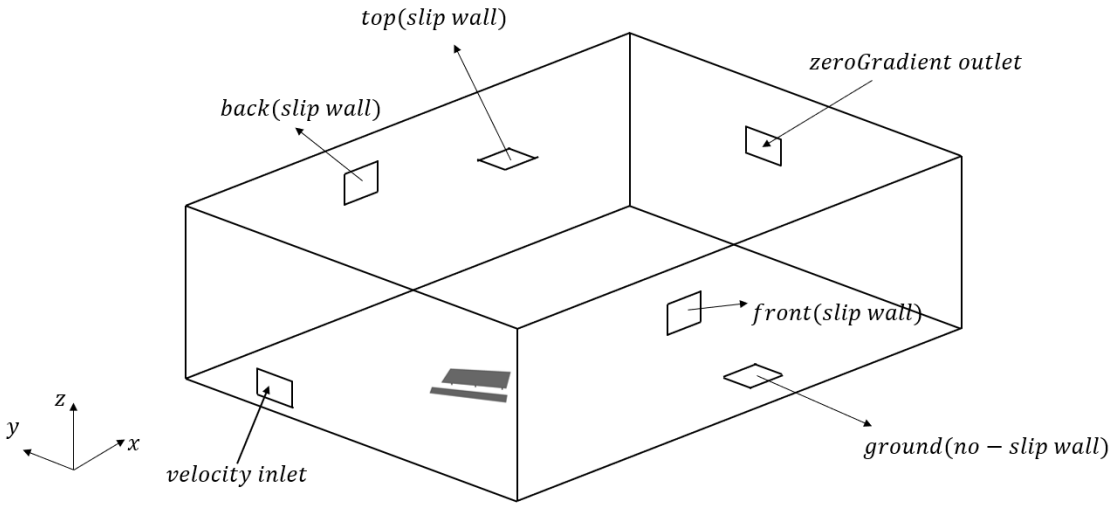

Figure 3. 5 Computational domain boundaries and axis descriptions

The freestream velocity (U_0) of 26 *m/s* is used based on the maximum mean hourly wind speed data recorded at London, Ontario airport [5]. The velocity profile is shown in Figure 3.7. The fluctuation in the *y* and *z* directions are not considered for the steady flow. This translates into a Reynolds number of 2.13×10^6 based on the wind speed at the module's lower edge height and the chord length of the module (W_M).

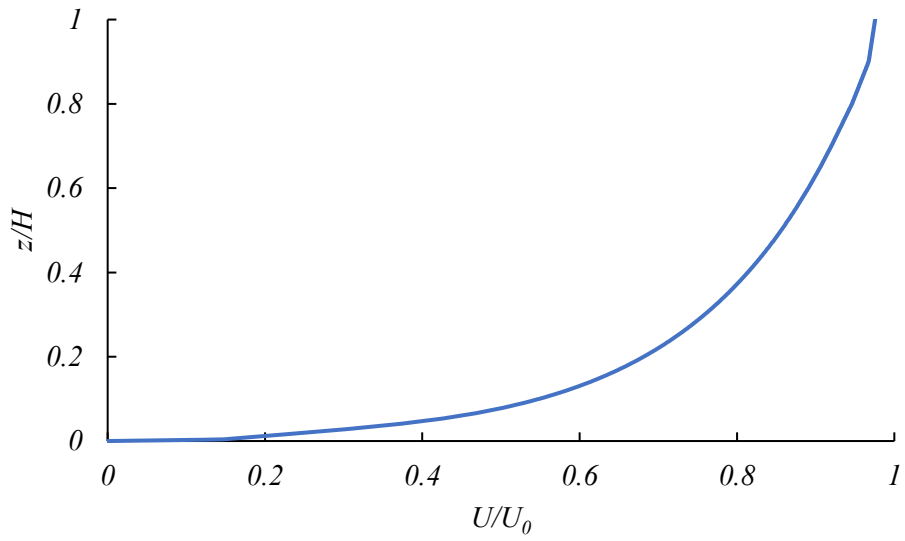

Figure 3. 6 Dimensionless inlet velocity profile

The outlet boundary of the domain is set as zeroGradient. The no-slip boundary condition is applied to all solid walls in the domain. The front, back, and top boundaries are set as slip walls, where the tangential component of the velocity at the boundary has the value of freestream velocity.

3.3.4 Computational Mesh Result and Simulating Time

The total cell number of 1.8 million is selected. Grid dependency tests were performed based on the cell number of 1, 1.5, 1.8, and 2 million, respectively. The net pressure coefficient value remains the same after reaching the cell number of 1.8 million. The net pressure coefficients on the PV module under wind direction 0° with different mesh cell numbers are shown in Table 3.3. The velocity profile from the center of the upper surface

of the module to the top of the domain is also compared, yet negligible differences are recognized within the domain under the tested range of the mesh numbers.

Table 3. 4 Computational mesh independency test results at cell number between 0.8 to 2.2 million

Cell number (million)	C_N	Error
0.8	1.14	-
1.1	1.06	7.55%
1.8	1.02	3.92%
2.2	1.02	very small

The multi-level mesh is applied to the close PV system to have a better prediction of the flow. The hexahedra and split-hexahedra mesh types are used in the domain, which is produced by using utility snappyHexMesh in OpenFOAM. The cross-section of the mesh results is shown in Figure 3.8.

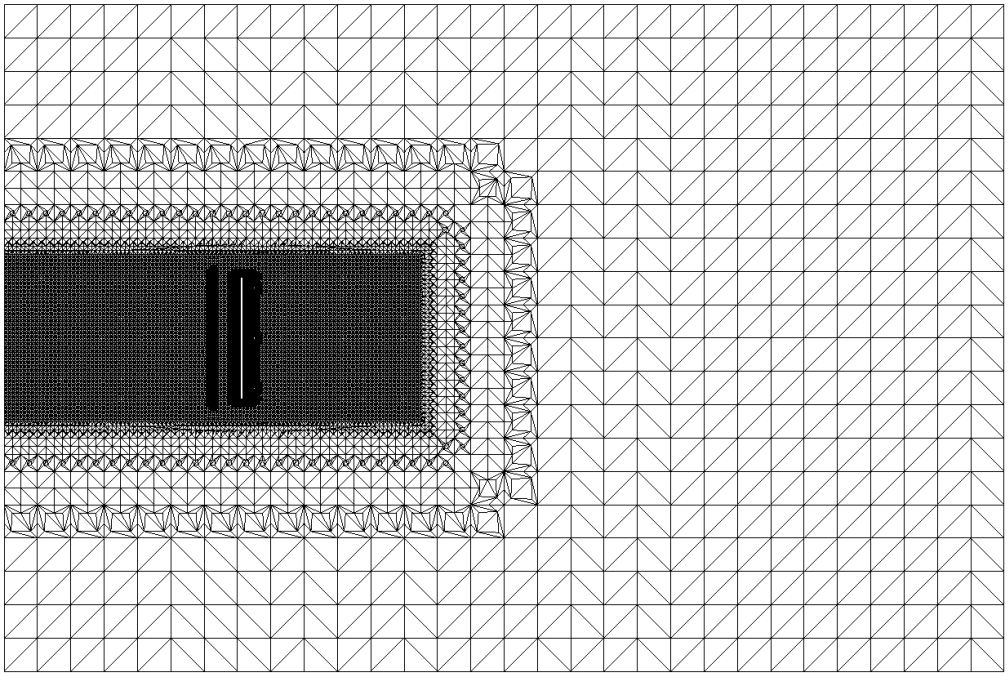

(a)

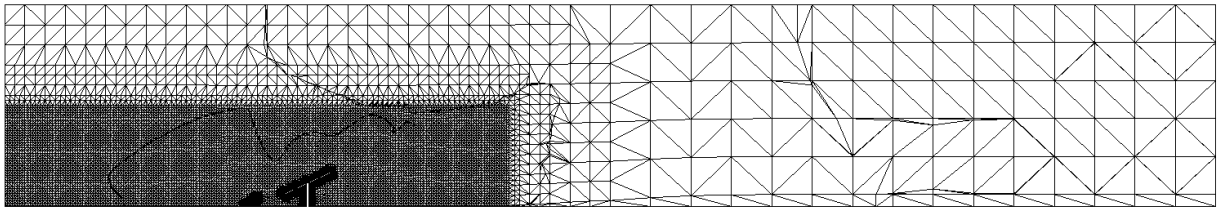

(b)

Figure 3. 7 (a) grids in multiple levels around the module and deflector, and (b) middle cross-section of the mesh

The simulations are mainly performed by the personal PC but also over the Graham cluster under ComputeCanada, using eight and 20 processors, respectively. The convergence criteria of 10^{-5} are employed for all variables. During the simulation, the time step size of 10^{-5} s is employed. A single simulation runs for an averaged total of 3 s of flow time, taking approximately 150 h to 400 h of elapsed real time to converge.

Chapter 4. RESULTS AND DISCUSSION

The purpose of the three-dimensional simulations is to predict the wind load changes after applying the flow deflector to the PV system. The wind load changes on the module are described using the net pressure coefficient (C_N), which is calculated using equation (4 - 1):

$$C_N = \frac{P_{upper} - P_{lower}}{0.5U_{ref}^2} \qquad (4-1)$$

where the pressures shown in the equation are kinematic pressure, which is defined as the pressure divided by the density (15 ℃ air in the current case, 1.225 kg/m^3), with the unit of m^2/s^2. The U_{ref} is the velocity at the reference height (0.6 m), which is 12 m/s. The default inclination angle θ of the PV module is 25° from the horizontal direction, and the gap size between the deflector and the edge of the PV module L_G is 0.5 W_M. The definition for the upper and lower surfaces is shown in Figure 3.4 (c). Drag and lift coefficients C_D and C_L are calculated using the following equations.

$$C_D = C_N cos(90 - \theta) \qquad (4-2)$$

$$C_L = C_N sin(90 - \theta) \qquad (4-3)$$

Here, θ is the inclination angle of the module shown in Figure 3.3 (b); the drag is acting against the flow, and the upward lift is considered positive [5]. A comparative study of

velocity distribution and turbulent kinetic energy (TKE) profiles in the domain is also performed. The results are presented along the centerline of the domain ($y = 0$) on different vertical lines. Figure 4.1 illustrates the positions of the vertical lines in the computational domain ($X = x/H$ = -0.6, -0.2, 0, 0.2, 0.6, and 1) where the distribution of the stream-wise velocity (U) is shown on the mid-plane (y = 0). The TKE profile is introduced to support the description of the velocity changes in the other two directions, y and z. Based on the assessment done in Ref [46], TKE can be predicted more accurately using SST $k-\omega$. An investigation of the accuracy of the turbulence models in predicting the C_N on the PV module is first performed in this chapter.

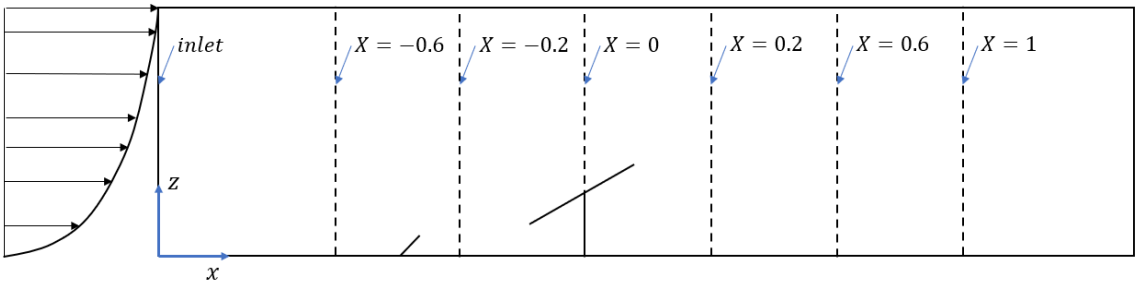

Figure 4. 1 Vertical position on the centerline of the domain ($y=0$)

4.1 Numerical Model Validations

4.1.1 Turbulence Model

It is critical to select a suitable turbulence model to calculate the flow properties accurately. The performance of the different RANS turbulence models in the prediction of the velocity and TKE near the object was tested in Ref. [46]. As shown in Figure 4.2, for the simulations of wind flow over a high-rise building, the SST $k-\omega$ turbulence model can predict the velocity and TKE more accurately in comparison to other turbulence models.

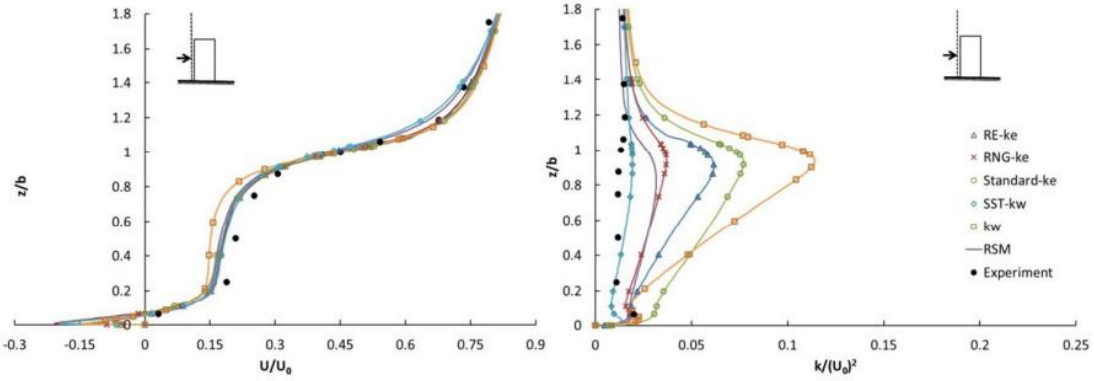

Figure 4. 2 Velocity profile (left), TKE profile (right) comparison with different turbulence model [46]

In the current study, different RANS models such as $k-\omega$, SST $k-\omega$, $k-\varepsilon$, RE, RNG, and RSM, are examined by the simulations of wind flow over a PV module at wind

direction 45°. C_N on the module is calculated and compared with the data in Ref. [5]. The comparison of the C_N values from the tested turbulence models is presented in Table 4.1.

Table 4. 1 Comparison of C_N on the module obtained from different turbulence models at wind direction of 45°

Turbulence model	C_N	Turbulence model	C_N
SST $k-\omega$	1.33	RE	1.30
$k-\omega$	1.95	RNG	1.33
$k-\varepsilon$	1.46	RSM	1.39

Comparing with the data obtained from Ref. [6], the SST $k-\omega$ turbulence model predicts the C_N within an acceptable range of error according to the validation results.

4.1.2 Aerodynamic loading (Benchmark solution)

Simulations are performed for a stand-alone PV module at wind directions of 0°, 45°, 135°, and 180°. The C_N values on the module are compared with Ref [5] in Figure 4.3.

Great agreements of the C_N values, together with the C_D and C_L values, are observed in Figure 4.3 (b).

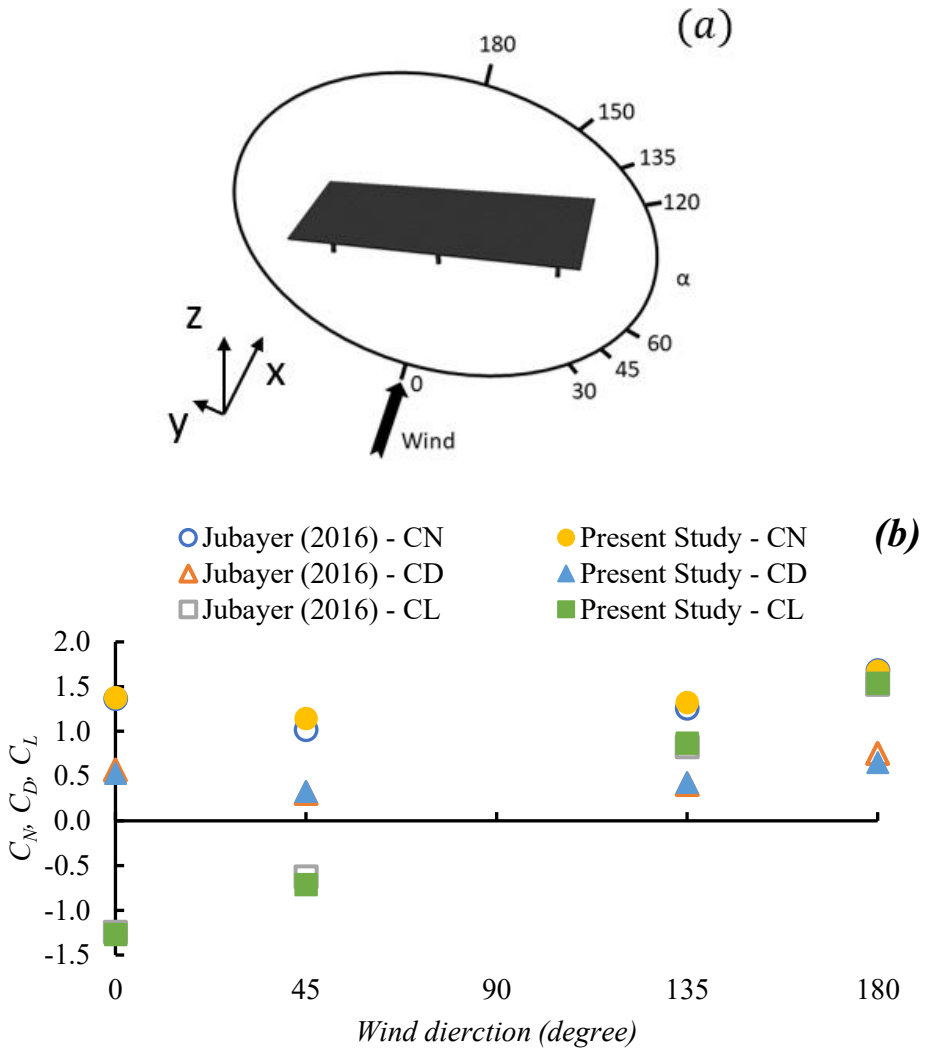

Figure 4. 3 (a) A schematic view of the wind flow directions over the stand-alone PV module, (b) C_N, C_L, and C_D on the module comparison between the current study and Ref. [5]

Almost identical coefficient values are found for 0° and 180° wind directions (less than 1% of difference), similarly for 45° and 135° wind directions (13% and 5% difference).

4.2 Flow Deflector Placed In Front of the PV Module

The purpose of using the flow deflector and the dimension of the deflector are introduced in the previous chapters. The role of the flow deflector on reducing the wind load on the PV module is examined in this section. A schematic view of the wind directions over the deflector-module combination is presented in Figure 4.4 to make clarification before the discussion of the results.

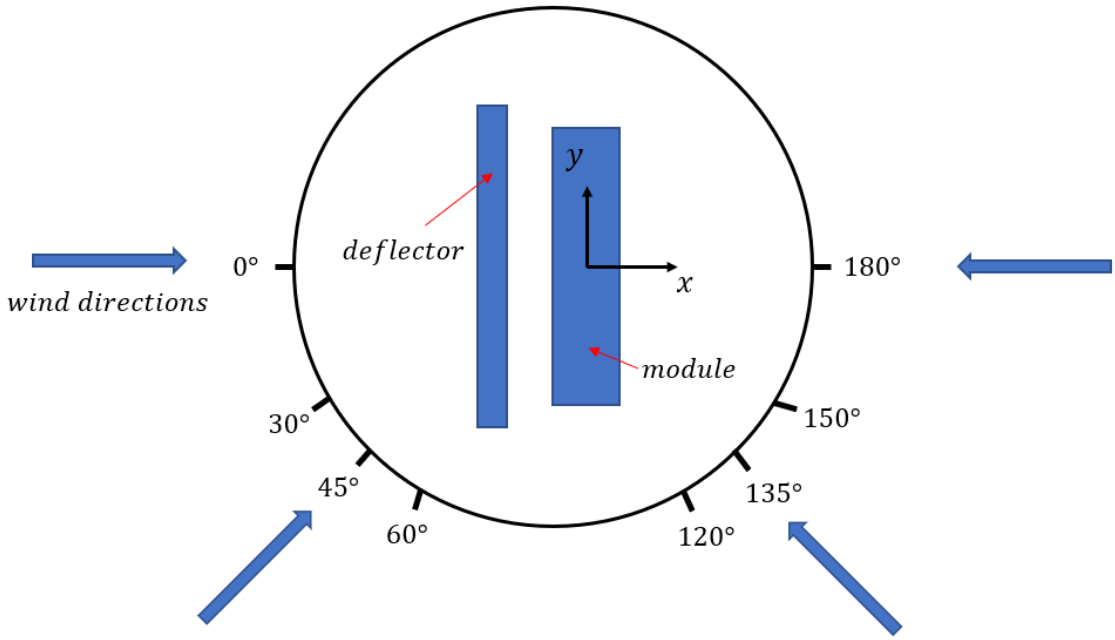

Figure 4. 4 A schematic view of wind flow directions over the deflector-module combination

A 3D overview of the velocity distribution under wind direction 0° is shown in Figure 4.5. The centerline (y = 0) and the reference height (h = 0.6) are marked, from where the data from the results are extracted.

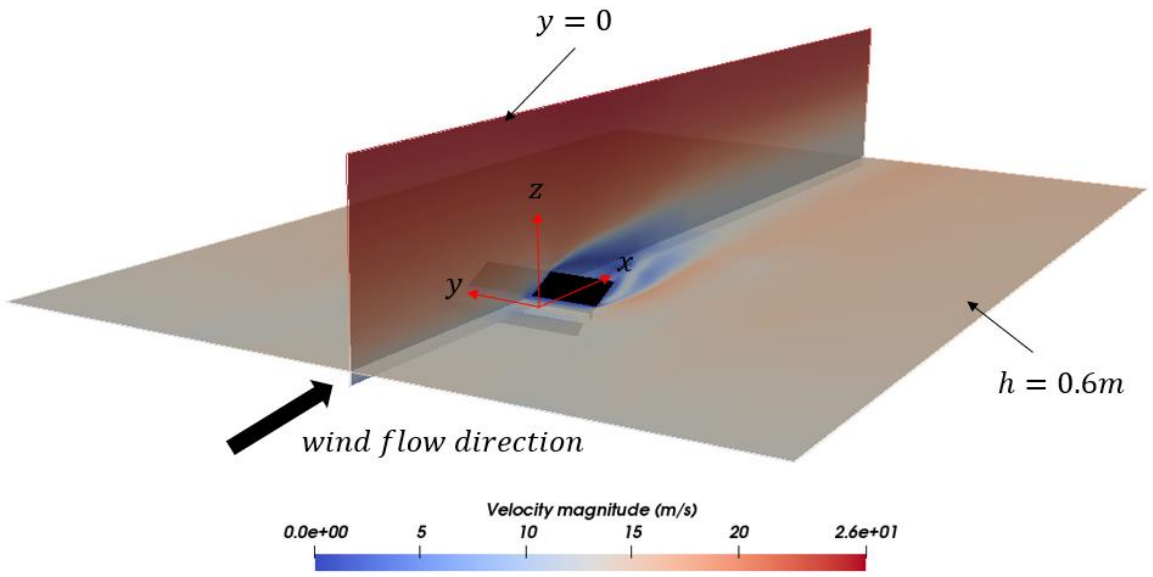

Figure 4. 5 3D velocity distribution view of the cross-sections of the centerline of the domain ($y=0$) and the reference height (h = *0.6 m*) for wind direction 0° with the deflector-module combination structure

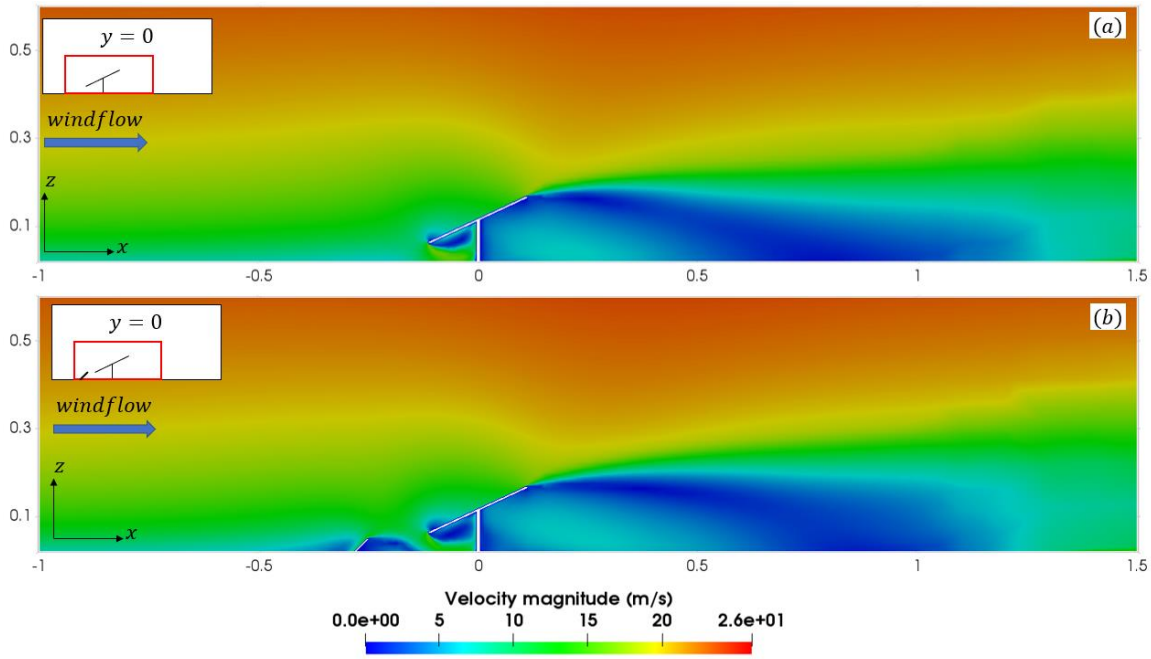

Figure 4. 6 Streamwise velocity distribution (a) without deflector and (b) with deflector under wind direction 0°

Figure 4.6 displays the streamwise velocity distribution at $y = 0$ with and without the flow deflector described by the rectangular inclined block in front of the module. Two separation zones (upper and lower) are created in the windward section of the PV module due to the no-slip wall boundary condition on the body of the module. After placing the flow deflector (Figure 4.6 (b)), this additional obstacle influences the stream direction, which results in the size changes of the separation zones. For the upper separation zone, the wind approaching the upper surface has been deviated, by which the reattachment point has been postponed, similar to the lower separation zone.

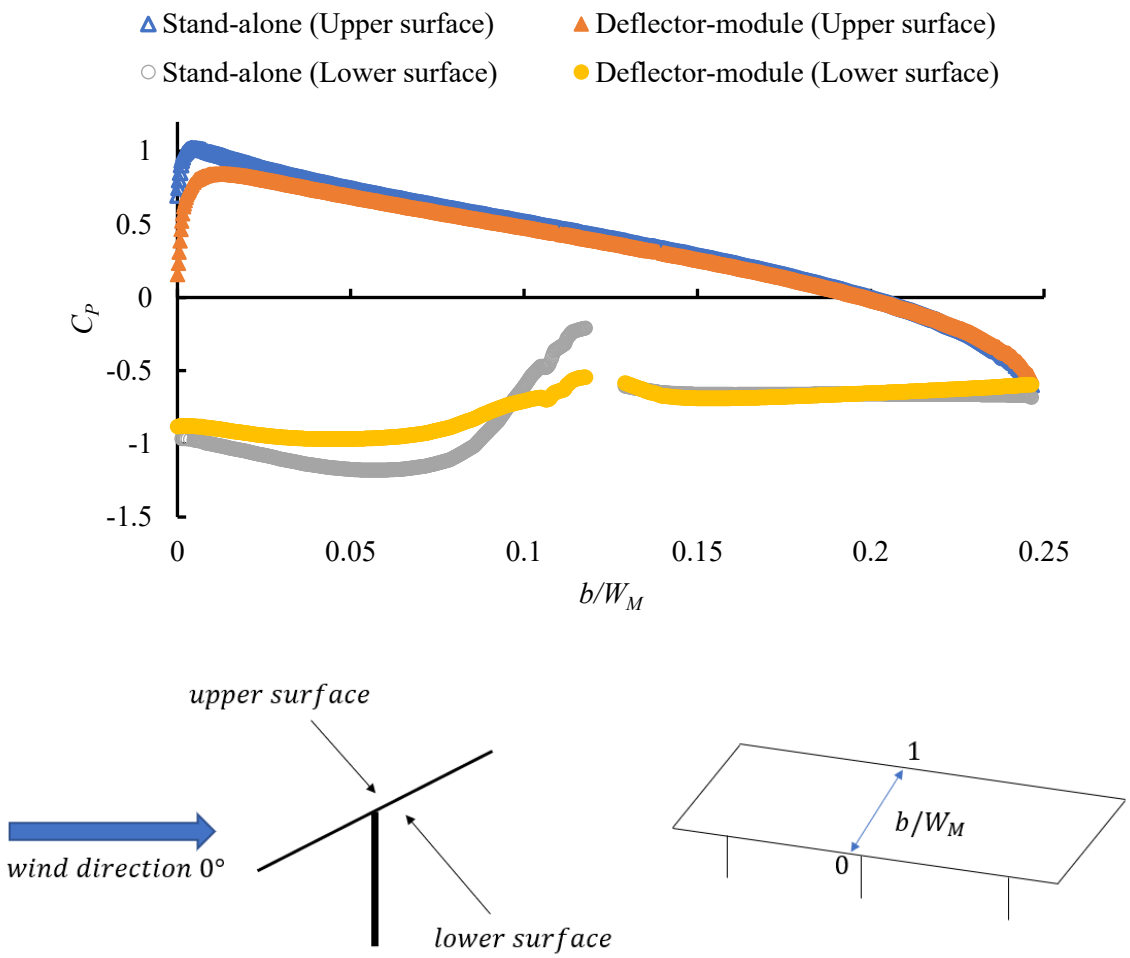

Figure 4. 7 Pressure coefficient distribution over mid-section of the windward surface of the module with and without the deflector (top), the definition of the wind direction and the surfaces (bottom left), and the schematic view of the midline, where *b* is the distance from the leading edge along with the breadth of the panel (bottom right) at wind direction of 0°

The distribution of the mean pressure coefficient is plotted in Figure 4.7 to investigate the pressure changes on the windward surface. Since the support structure (pillar) is considered in the current study, no pressure data is collected within the pillar, which reveals

by the discontinuous pressure distribution on the lower surface of the module. Reference pressure and wind speed for calculating C_P are taken at the same location as Ref. [6] in order to make the comparison meaningful ($C_P = (P - P_{H=0.82})/(0.5 \times U_{H=0.82}^2)$). Pressure distribution on the upper section of the surface shows little difference ($0.5 < b/W_M < 1$), which matches the little difference in the streamwise velocity distribution changes near this section that are shown in Figure 4.6. A significant pressure reduction is observed close to the lower windward edge of the module, which also matches the streamwise velocity distribution changes on both sides of the module. To be noticed that the pressure reduction on the upper surface mainly close to the leading edge of the module ($0 < b/W_M < 0.02$), but the pressure reduction on the lower surface at the lower section is consistent ($0 < b/W_M < 0.12$), which suggests reduced drag on the module. Along the mid-section of the module, the maximum pressure on the upper surface is reduced by 16.67%, and the maximum pressure on the lower surface is reduced by 17.80%.

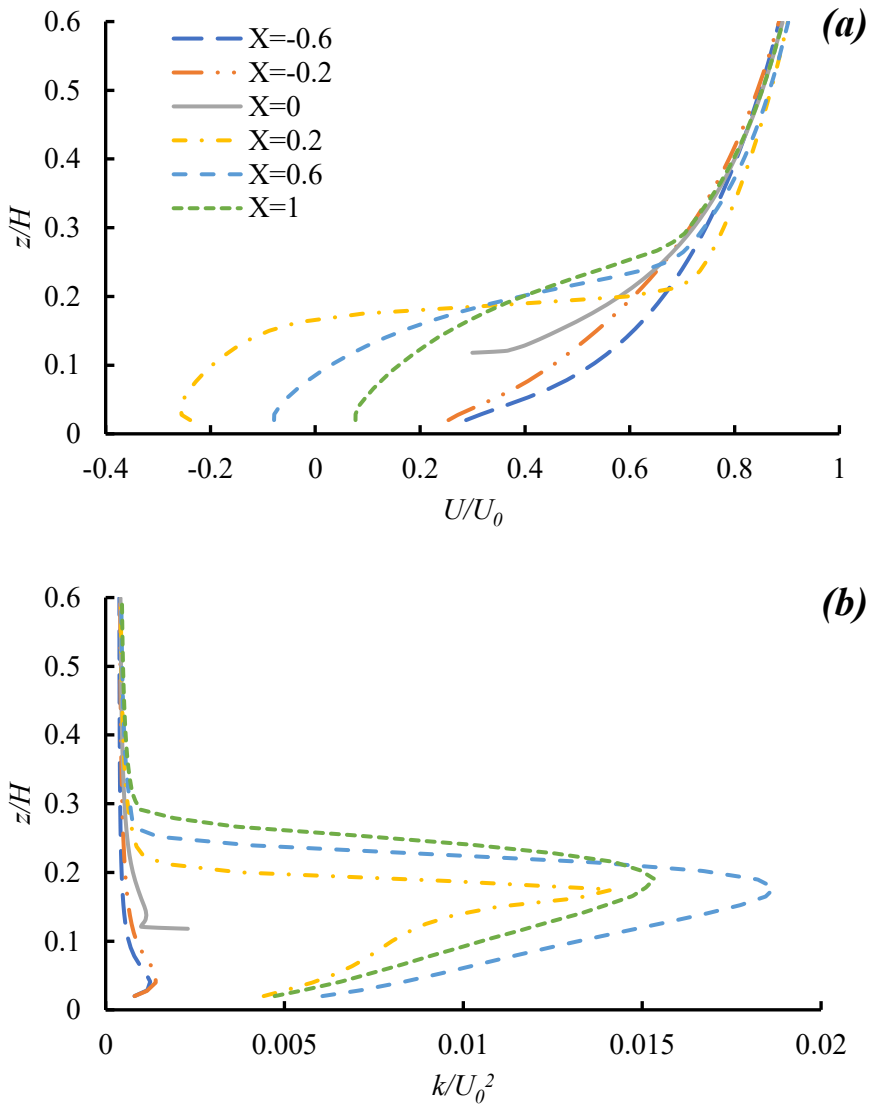

Figure 4. 8 (a) Streamwise velocity distribution and (b) TKE profile near the stand-alone PV module without the deflector under wind direction 0° at X = -0.6, -0.2, 0, 0.2, 0.6, 1

Figure 4. 8 (a) The streamwise velocity distribution at different sections in the computational domain. The developed flow is observed at the upstream ($X < 0$) of the module, where the profile is very similar to the inlet velocity profile (Figure 3. 6a). The

flow recirculation takes place at the downstream of the module, which is recognized at X = 0.2 and 0.6. Yet overviewing the velocity distribution from X = 0 to 1, the flow gradually recovers itself by moving farther to the downstream of the module. The TKE value reaches the maximum of 0.0142 at X = 0.2, 0.0187 at X = 0.6, and 0.0153 at X = 1, which are shown in Figure 4.8 (b).

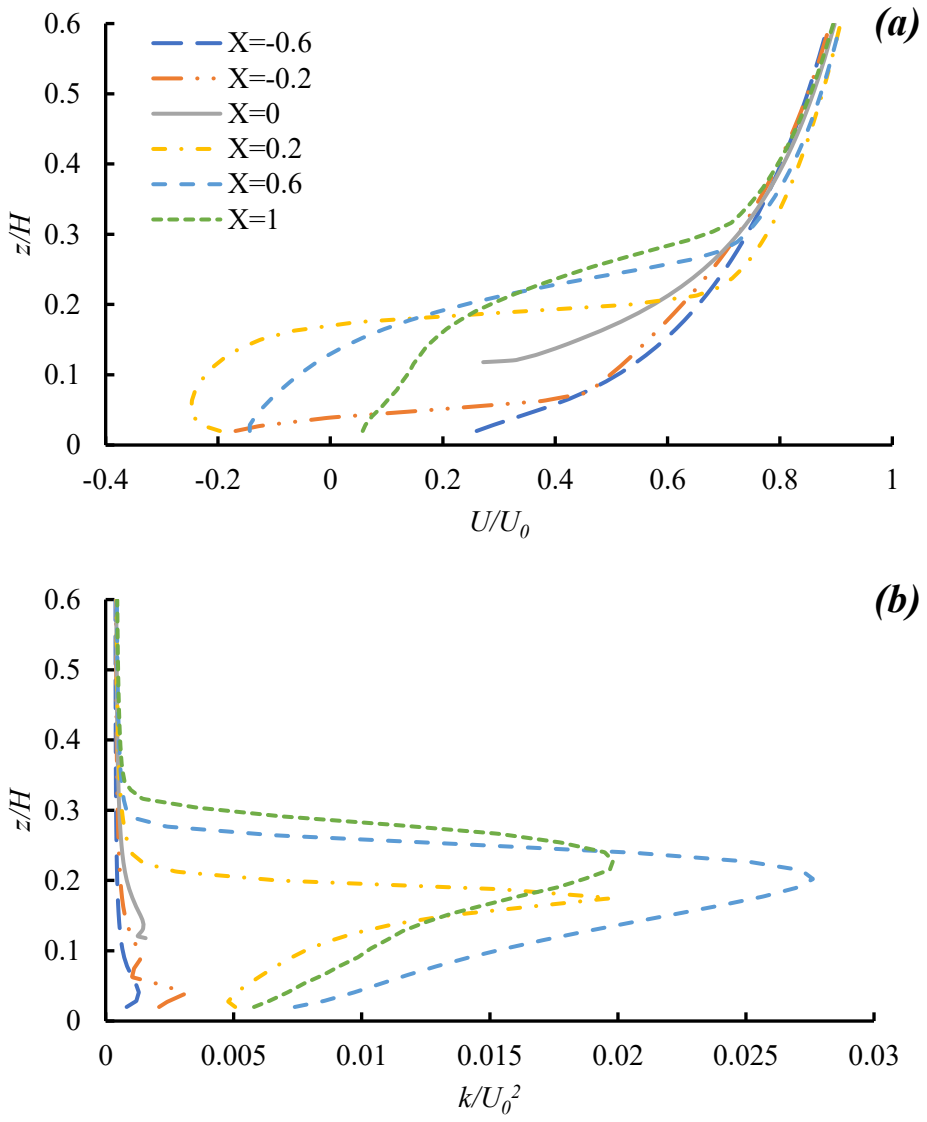

Figure 4. 9 (a) Streamwise velocity distribution and (b) TKE distribution for a PV module with a flow deflector in the front under wind direction 0° at X = -0.6, -0.2, 0, 0.2, 0.6, 1

A similar pattern of the distribution of the streamwise velocity is observed at the upstream of the module in Figure 4.8 (a) and 4.9 (a) (X = -0.6). However, a new recirculation zone is created at the downstream of the deflector, which is also upstream of

the module (X = -0.2) when the lower stream encounters the deflector. Correspondingly, a significant x velocity changes from U/U_0 = 0.4 to -0.2 (reverse in direction) is observed at X = -0.2. After applying the flow deflector (Figure 4. 9b), the TKE profile does not change at the upstream far from the module (X < -0.6). However, after the flow encounters the module (-0.6 < X < -0.2), the TKE increases alongside the U reduction in the recirculation region, which is created by the deflector (X = -0.2). A similar pattern of the streamwise velocity distribution and TKE profile changes is observed at the downstream of the module, where the U decreases within X = 0.2 to X = 0.6, while the maximum TKE increases by 30% (velocity increase in the other two directions), shown in Figure 4.8 (b) and 4.9 (b). The flow gradually recovers itself, which is again observed in a similar velocity distribution shown between Figure 4.8 (a) and 4.9 (a) at the downstream of the module (X > 0). The flow streamlines are further identified in Figure 4.10.

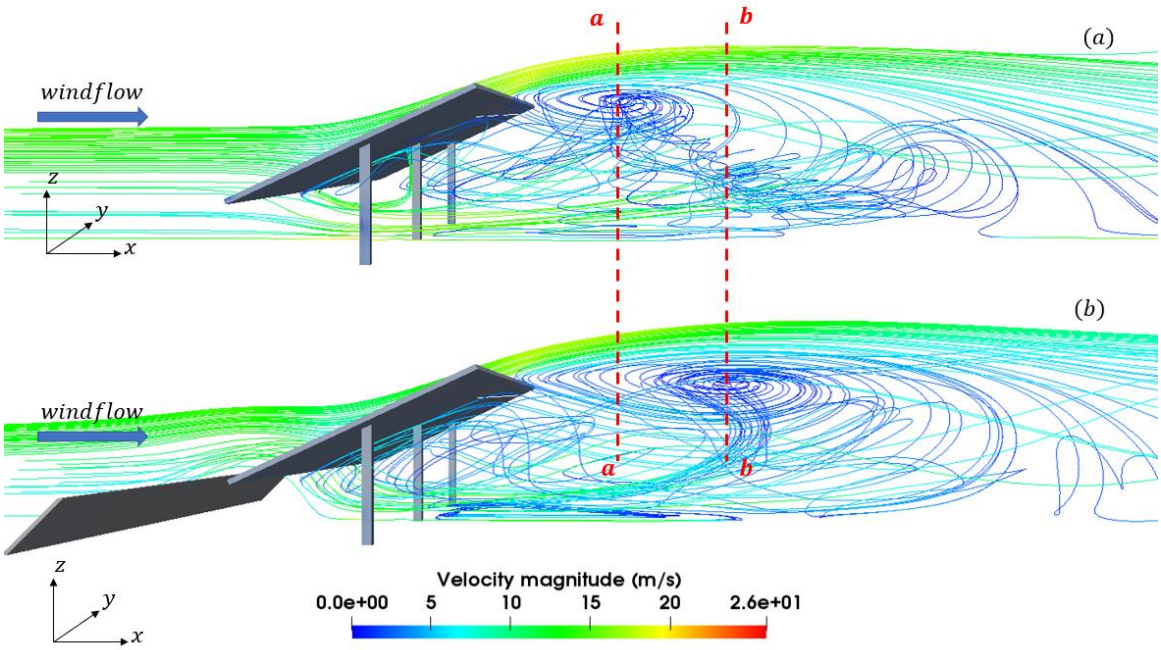

Figure 4. 10 Flow streamlines near the PV module (a) without and (b) with the flow deflector under wind direction 0°

It is noticed in Figure 4.10 that the centre of the recirculation region moved farther away from the module (*a*-*a* to *b*-*b*) due to the presence of the additional obstacle at the upstream of the module, which leads to the changes in the wind flow streamlines and the separations at the edges of the PV module. The streamlines near the module reveal that the centre of the recirculation region is shifted farther away from the module to the downstream after applying the deflector, which suggests a reduction of the drag on the module. The changes in the pressure on the surfaces and the C_N value on the module are compared in Table 4.2.

Table 4. 2 Surface pressure and C_N on the module under wind direction 0° with and without the flow deflector in front of the module

	upper surface pressure	lower surface pressure	C_N
without flow deflector	18.22	-81.06	1.38
with flow deflector	10.31	-71.97	1.11

Table 4.2 shows that the pressure on the windward surface reduces by 43.4% after applying the deflector, while it reduces by 11.2% at the leeward surface of the module. The windward surface pressure reduction matches the reduction of the TKE, while the x component of the velocity remains almost the same, which was previously shown in Figures 4.8 and 4.9. C_N on the module reduces by 17.12% in total.

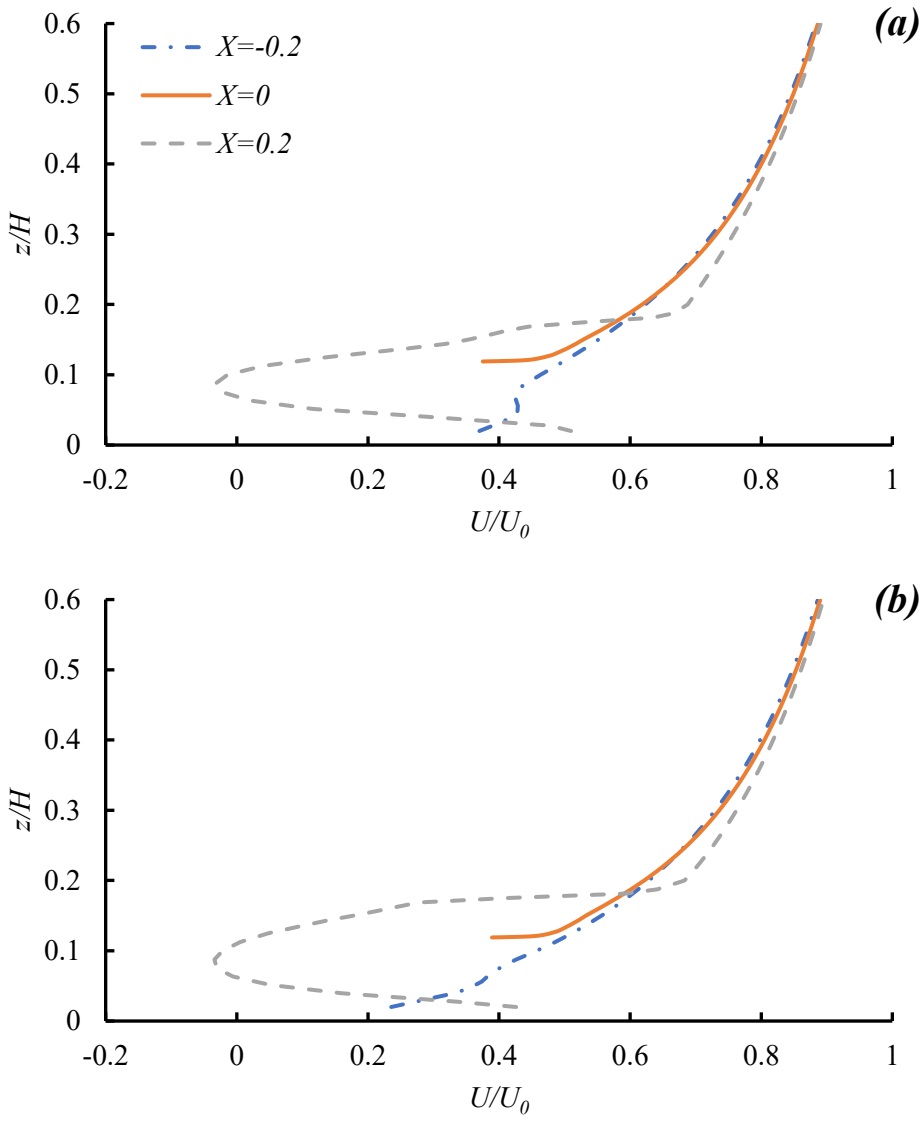

Figure 4. 11 Velocity distribution in the *x*-direction for a PV module under wind direction 45° (a) without the deflector and (b) with the deflector

Figure 4.11 illustrates the vertical distribution of the velocity in the *x*-direction, where the module is at 45° with respect to the wind direction. According to the streamwise velocity distribution at the center of the domain ($y = 0$), the flow is not significantly affected

by the presence of the deflector under such wind direction (45°) except for the flow upstream of the module (X = -0.2). Since the deflector is not directly facing the stream, the recirculation region downstream of the deflector is barely changed at the centerline of the domain downstream of the module (X = 0.2). Yet the presence of the deflector still has an impact on the wind flow direction upstream of the module, which leads to a velocity reduction in the x-direction upstream of the module (X = -0.2). The minimum velocity drops from 9.62 *m/s* to 6.13 *m/s* is observed between Figure 4.11 (a) and (b). Due to the same reason, the velocity in the x-direction shows a very similar pattern above and at the downstream of the module.

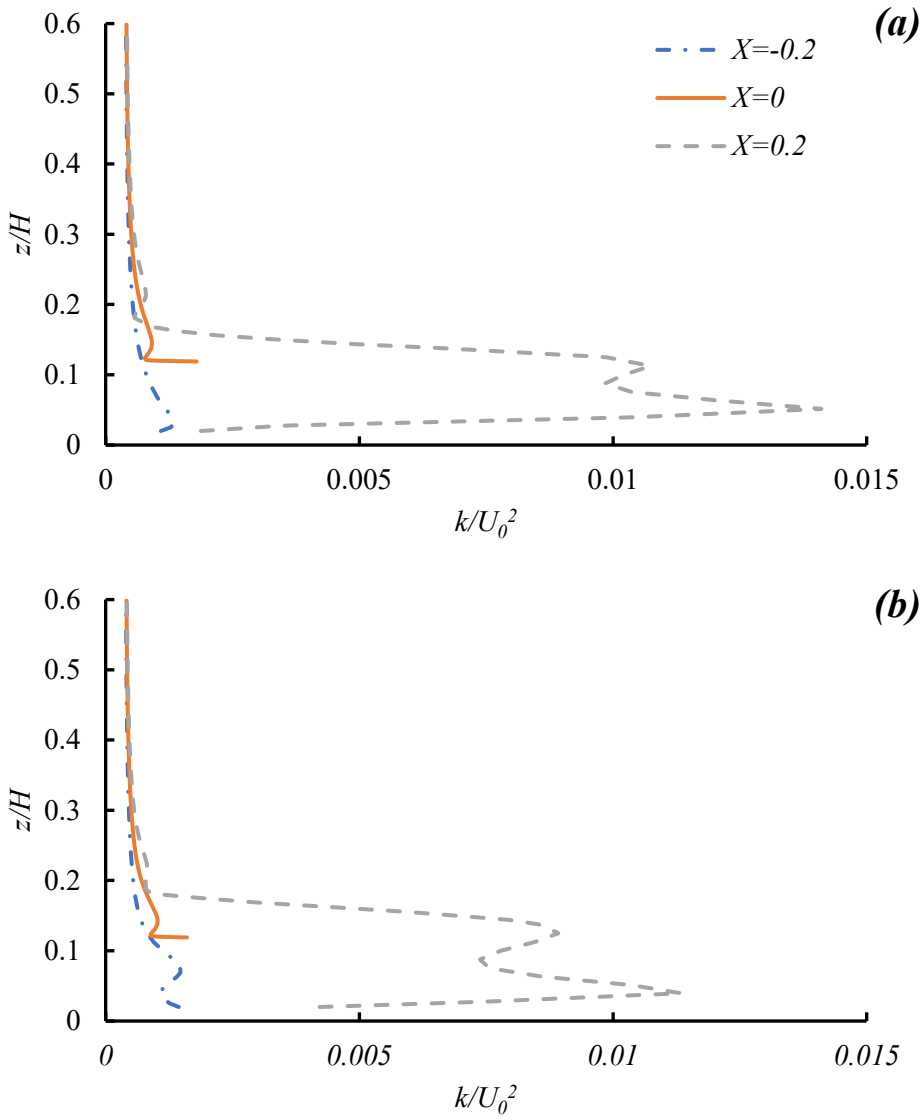

Figure 4. 12 TKE distribution for a PV module under wind direction 45° (a) without the deflector and (b) with the deflector

The maximum TKE increases from 0.89 m^2/s^2 to 0.996 m^2/s^2 observing from Figure 4.12. Before applying the deflector, the maximum TKE, which is shown in Figure 4.12 (a), is close to 10 m^2/s^2 at X=0.2 and in the domain. After applying the deflector, the maximum

TKE at the same location drops to 8 m^2/s^2, while the recirculation region of the flow expands in height from 0.03 (z/H = 0.07 to 0.102) to 0.045 (z/H= 0.062 to 0.1092). However, compared with the velocity distribution and TKE changes for the PV system under a wind direction of 0°, the influence brought by the presence of the deflector on the wind behavior near the module is very limited in a wind direction of 45°.

Table 4. 3 Surface pressure and C_N on the module under wind direction 45° with and without the flow deflector in front of the module

	upper surface pressure	lower surface pressure	C_N
without flow deflector	9.82	-72.66	1.15
with flow deflector	7.86	-71.07	1.10

Table 4.3 shows the pressure on the windward surface reduces by 19.96% after applying the deflector while it reduces by 2.19% at the leeward surface of the module. C_N on the module is reduced by 4.30% in total. However, the deflector in front of the module is not directly facing the stream; therefore, the worse performance of the deflector is expected where the C_N reduction at 45° is less than at 0° wind direction.

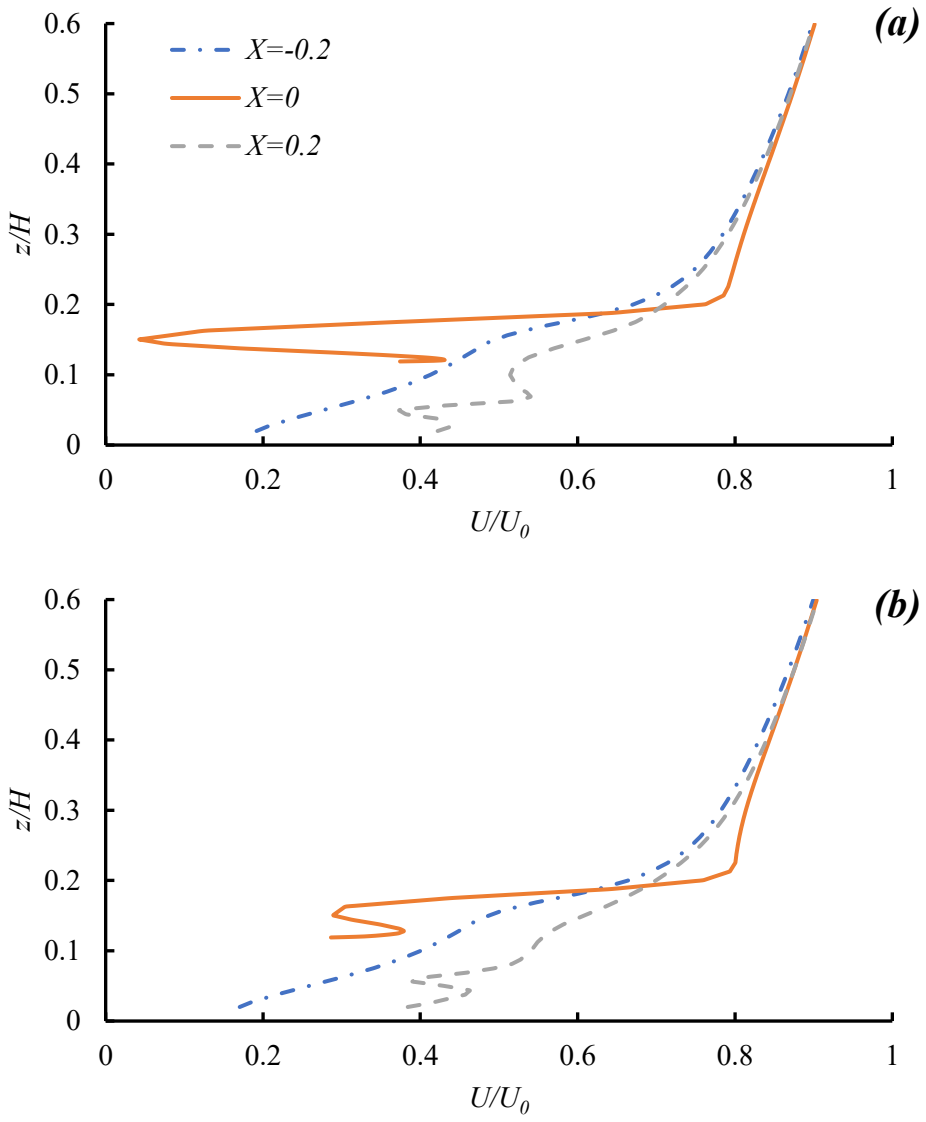

Figure 4. 13 Velocity distribution in the *x*-direction for a PV module under wind direction 135° (a) without the deflector and (b) with the deflector

Since the deflector is at the downstream of the module under a wind direction of 135°, the flow at the upstream of the module shows little difference between Figure 4.13 (a) and (b) (X = -0.2). The x velocity near the upper surface of the module increases significantly

($X = 0$), which suggests that the behavior of the flow at the downstream of the module has been changed by the presence of the deflector.

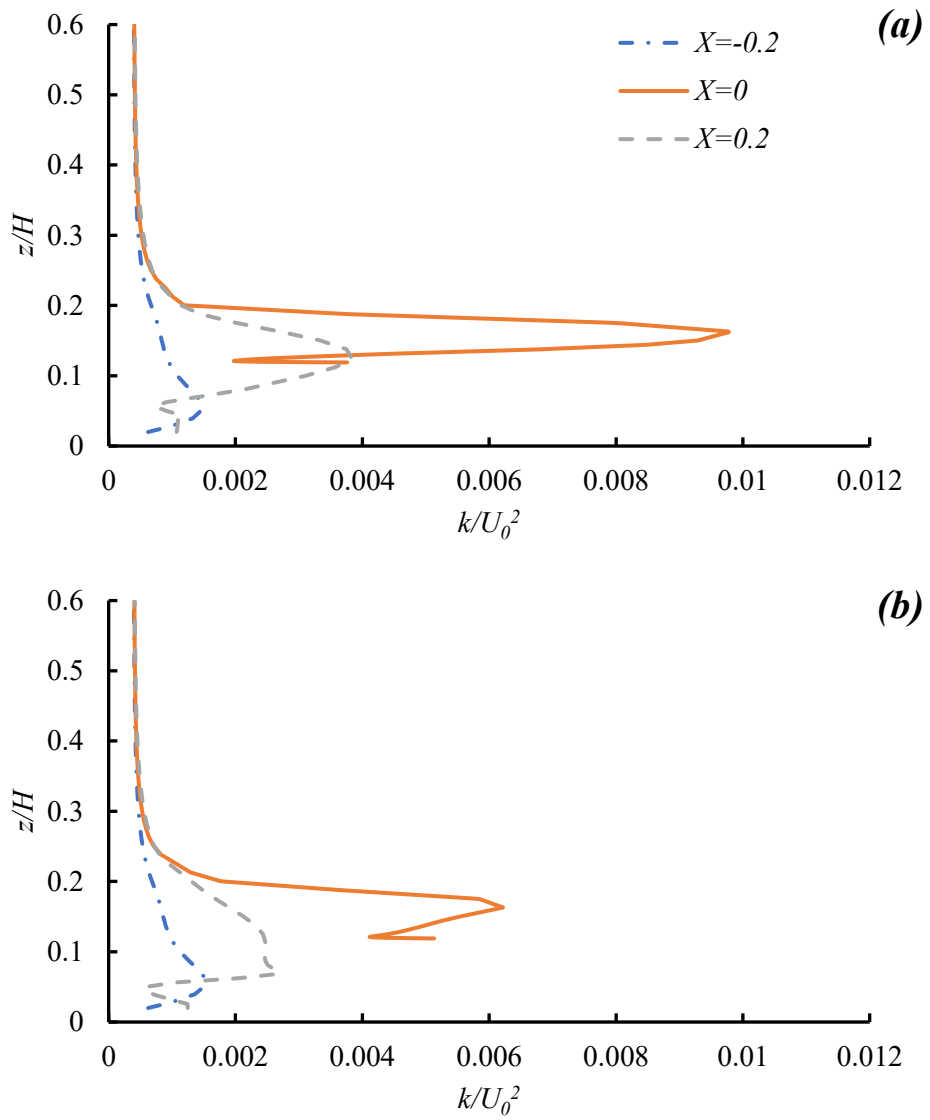

Figure 4. 14 TKE distribution near the PV module at $y = 0$ under wind direction 135° (a) without the deflector and (b) with the deflector

The TKE is reduced by 36% from a maximum of 6.61 m^2/s^2 to 4.22 m^2/s^2 due to the presence of the deflector under a wind direction of 135, which is shown in Figure 4.14 (a) and (b). However, the amount of the TKE difference remains at a relatively low level (reduced by 2.39 m^2/s^2). Therefore, a similar pattern is expected as the C_N changes under a wind direction of 45°, in which the presence of the deflector affects the flow behavior near the module, yet the influence is not significant since the deflector is not facing the wind direction.

Table 4. 4 C_N on the module under wind direction 135° with and without the flow deflector in front of the module

	C_N
without flow deflector	1.32
with flow deflector	1.28

A 3.03% wind load reduction is found on the PV module after applying the flow deflector under a wind direction of 135° in Table 4.4. However, the wind load reduction brought by the existence of the deflector at the downstream of the module is revealed by the C_N that the performance of the deflector is very limited when the deflector is not facing the wind direction.

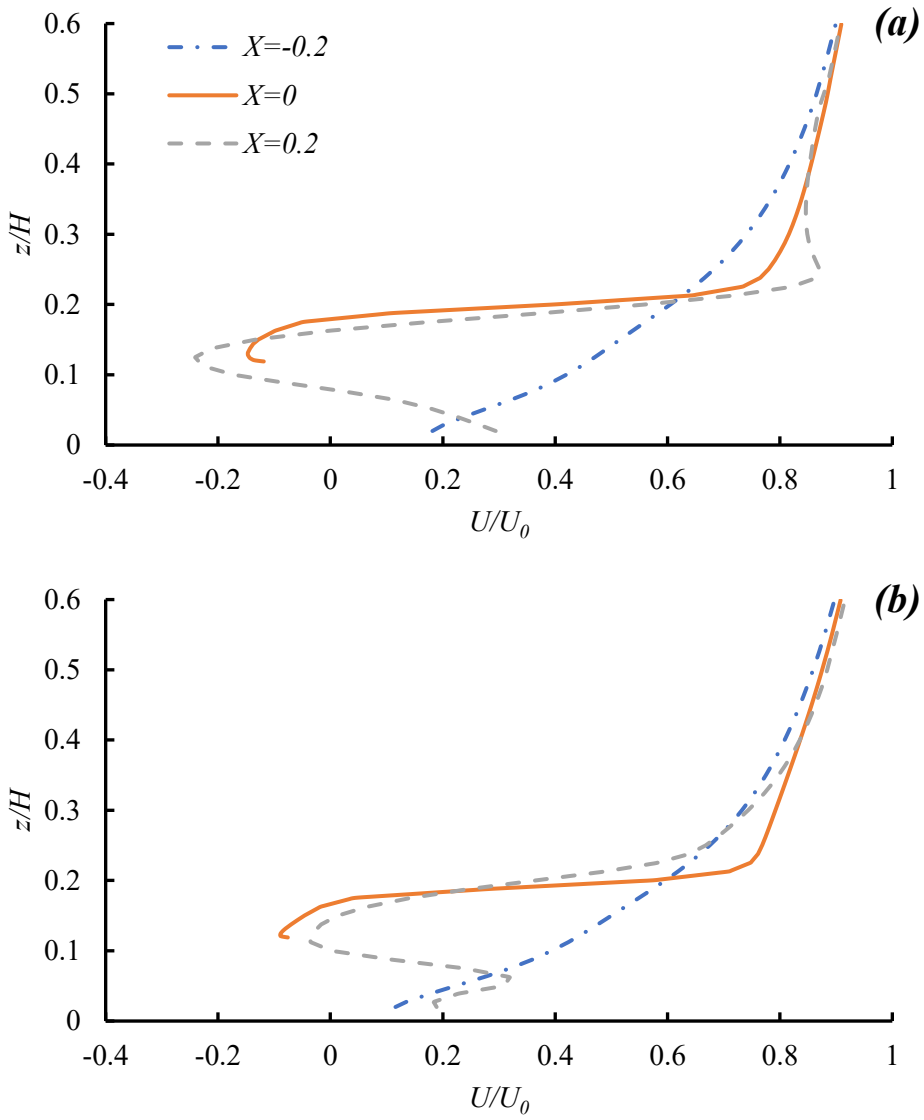

Figure 4. 15 Streamwise velocity distribution near a PV module at $y = 0$ under wind direction 180° (a) without the deflector and (b) with the deflector

Figure 4.15 (a) and (b) illustrate the distribution of the velocity in the x-direction near the module. The upstream of the flow shows an almost identical distribution since the deflector is at the downstream of the module ($X = -0.2$). For the flow field at the leeward side of the stand-alone module ($X \geq 0$), the recirculation region between $X = 0$ (above the

module) and X = 0.2 (near the downstream side of the module) is observed from the velocity distribution in Figure 4.15 (a). The presence of the deflector changes the recirculation region near the upper surface of the module, which is revealed from the streamwise velocity distribution shown in Figure 4.15 (b). The reduction of the velocity near the upper surface of the module indicates that the center of the recirculation region is shifted closer to the module with the presence of the deflector at the downstream, which suggests an increase of the uplift on the module.

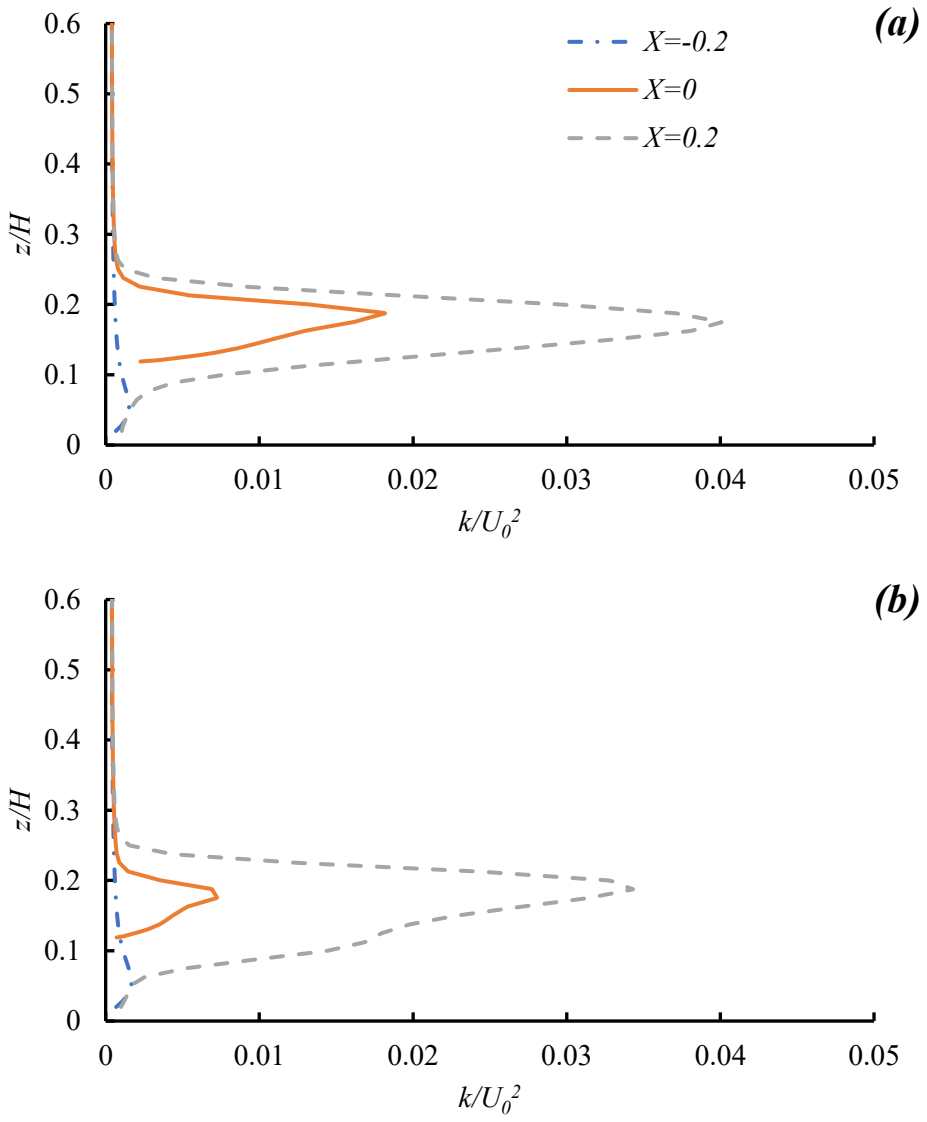

Figure 4. 16 TKE distribution near a PV module under wind direction 180° (a) without the deflector and (b) with the deflector

A similarity change of the TKE is found again at the downstream of the module after applying the deflector in Figure 4.14 and Figure 4.16. The TKE shows a very similar profile at the upstream of the module (X = -0.2). While at the downstream of the module (X = 0,

0.2), the TKE decreases from 12.289 m^2/s^2 to 4.8983 m^2/s^2 at X = 0 and 27.09 m^2/s^2 to 23.199 m^2/s^2.

Table 4. 5 Surface pressure and C_N on the module under wind direction 180° with and without the flow deflector in front of the module

	C_N
without flow deflector	1.68
with flow deflector	1.40

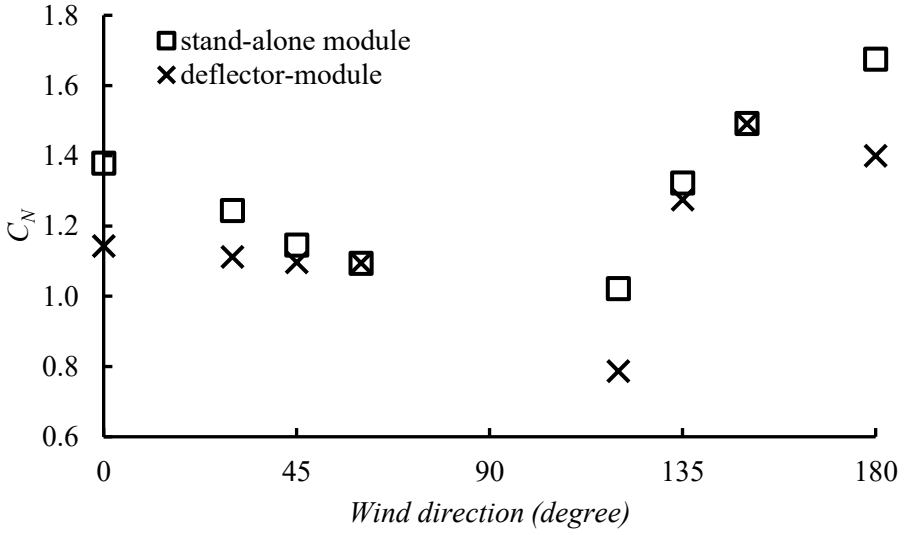

Figure 4. 17 The C_N on the PV module before and after adding the flow deflector in front of the module

An effective reduction of the wind load after applying the deflector is observed from Figure 4.17. The C_N reduction under each wind direction is further addressed and discussed in Table 4.6.

Table 4. 6 C_N comparison with and without the deflector in front of the PV module

wind direction	C_N without deflector	C_N with deflector	Load reduction
0°	1.38	1.14	17.12%
30°	1.24	1.11	10.61%
45°	1.15	1.10	4.30%
60°	1.09	1.09	0.01%
120°	1.02	0.79	23.03%
135°	1.32	1.28	3.61%
150°	1.49	1.49	0.06%
180°	1.68	1.40	16.42%

The maximum wind load reduction reaches 23.03% after applying the deflector in front of the stand-alone module. For the wind directions 0°, 45°, 135°, and 180° [5], the wind load is reduced from a minimum of 3.61% to a maximum of 23.03%, respectively.

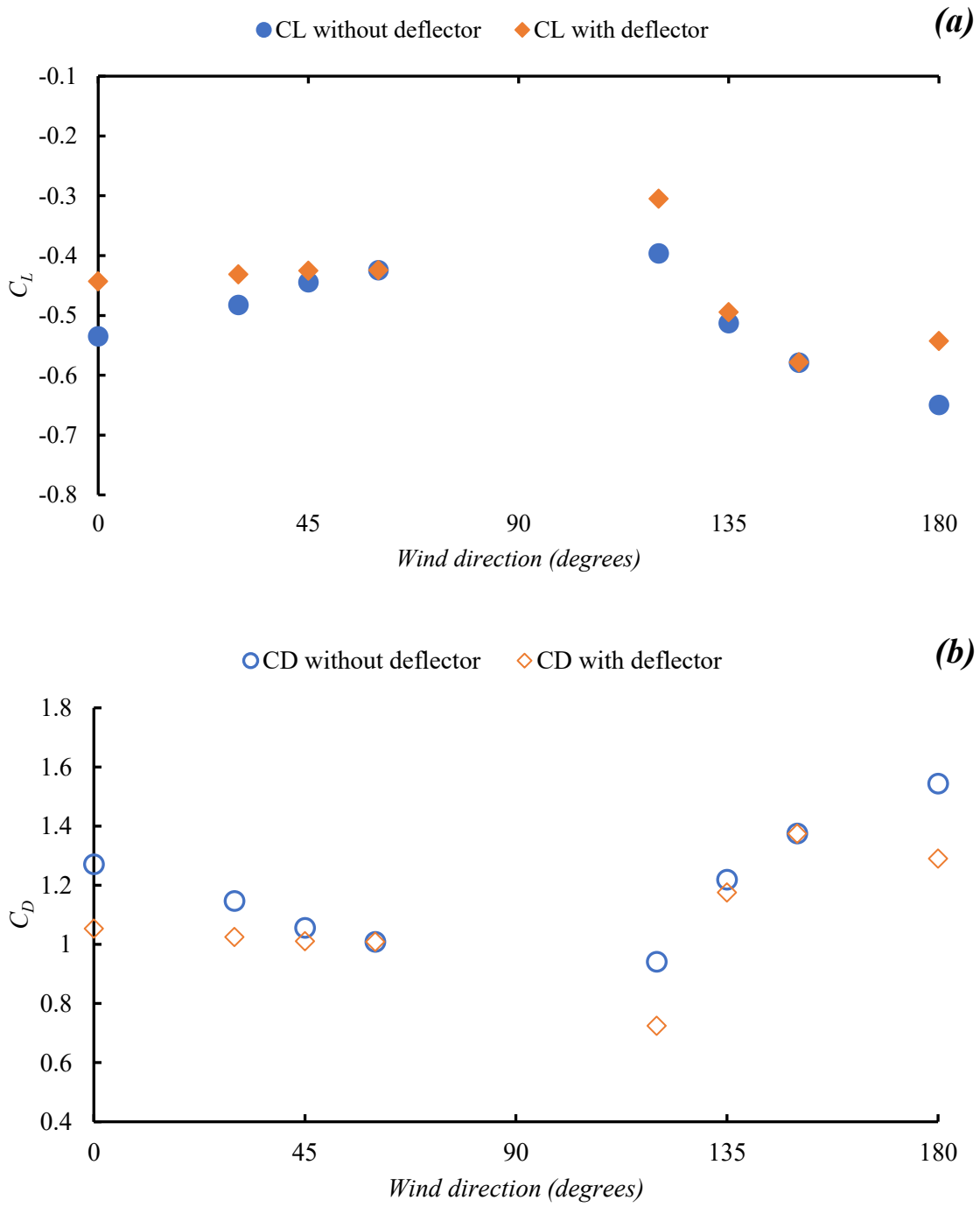

Figure 4. 18 (a) C_L and (b) C_D with and without the deflector in front of the stand-alone PV module

The drag and lift coefficients shown in Figure 4.18 has the same pattern as C_N, except for a wind direction of 180°. Both the drag and lift coefficients are reduced by different levels after applying the deflector in front of the stand-alone module. However, the reduction of the C_D is more than C_L. For instance, in wind direction 0°, while the C_N reduced from 1.38 to 1.14, the C_D reduced from 1.27 to 1.05 (by 22%), and the C_L reduced from -0.53 to -0.44 (by 9%). As stated in Figure 4.8, the deflector changes both upstream and downstream flow in wind direction 0°, which results in a more significant reduction of drag and a slight decrease in lift. A similar pattern of coefficients due to the presence of the deflector in front of the module at upstream is also seen in the wind direction of 45° where the C_N reduces from 1.24 to 1.11, where the C_D reduced from 1.06 to 1.01 by 4.54%, and the C_L reduced from 0.44 to 0.43 by 1.91%. While the deflector is at the upstream of the module, the impact on the streamlines is very limited since the lift is only reduced under 10%. Also, the effectiveness of the deflector is weakened when it shifts away from directly facing the stream direction.

4.3 Flow Deflector Placed Around the PV Module

As known from the previous section that the performance of the flow deflector on the wind load reduction on the module is weakened from wind direction 0° to 150° since the deflector is shifting away from facing the wind direction. Therefore, in order to maximize the wind load reduction performance using the flow deflector, the wind load changes on the PV module with a deflector facing the stream direction under wind directions from 0° to 180° are discussed in this section. The schematic view of the wind directions over the current deflector-module combination is presented in Figure 4.19.

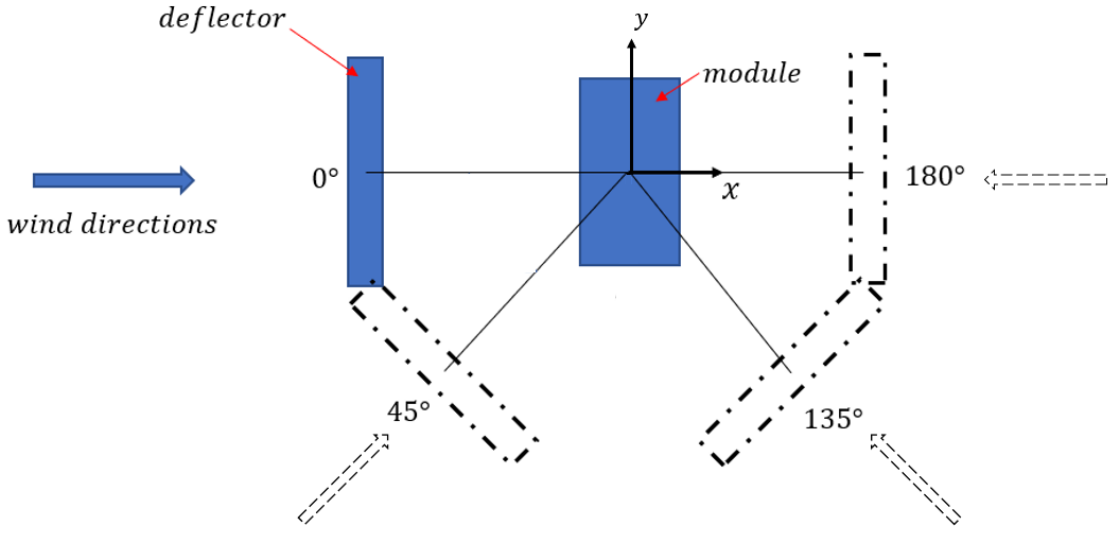

Figure 4. 19 A schematic view of wind flow directions over the deflector-module combination

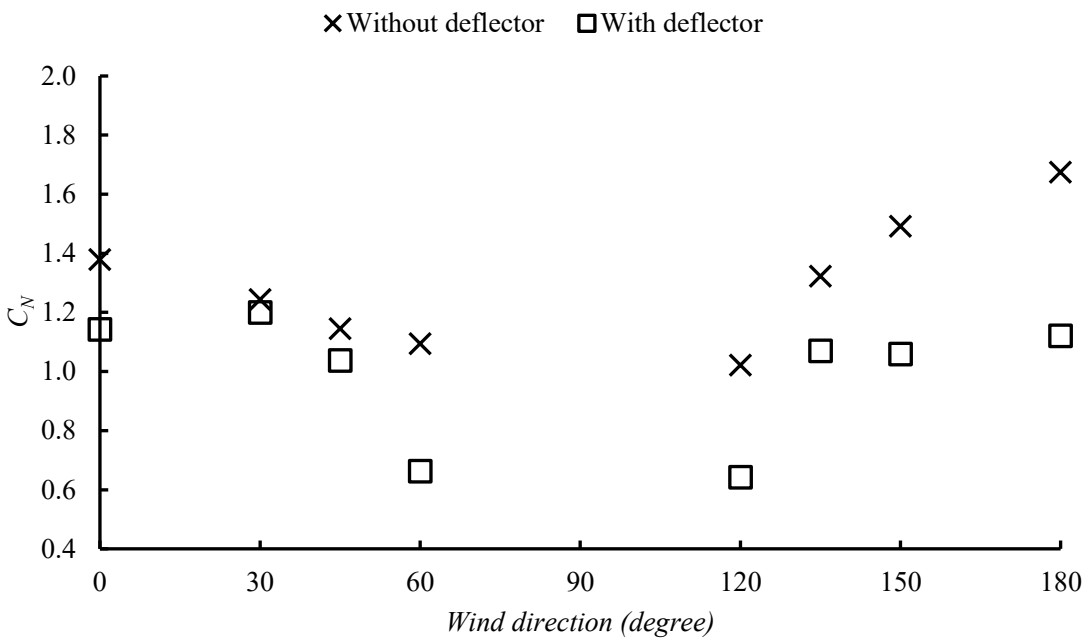

Figure 4. 20 Comparison of the C_N on the PV module with and without the deflector placed around the module

Table 4. 7 C_N comparison with and without the deflector placed around the PV module

wind direction	C_N without deflector	C_N with deflector	Load reduction
0°	1.38	1.14	17.12%
30°	1.24	1.20	3.48%
45°	1.15	1.04	9.37%
60°	1.09	0.66	39.36%
120°	1.02	0.64	37.10%
135°	1.32	1.07	19.05%
150°	1.49	1.06	29.97%
180°	1.68	1.12	33.03%

As observed in Figure 4.20 in support of the values offered in Table 4.7, placing the deflector facing the wind direction around the stand-alone module contributes to a greater C_N reduction on the module compared with the C_N on the module with the deflector in front. Unlike the performance of the deflector faded with the increase of the wind direction, the C_N obtained from the module with the deflector facing the wind direction is similar to the C_N distribution pattern on the stand-alone module. The increase in the reduction of the C_N is observed within wind directions from 120° to 180°, where the module upper surface is at the downstream compared with the data provided in Table 4.6. For instance, at a wind direction of 135°, the C_N on the module is 1.32 without the deflector, which is reduced by placing the deflector in front of the module to 1.28, while adjusting the deflector to face the wind direction reduces the C_N to 1.07. The maximum C_N is reduced from 1.68 to 1.20 by 28.57%, 17.26% more than the maximum C_N reduction when the deflector is in front of the module.

4.4 Different Spacing L_G

The gap size between the edge of the deflector and the module is another factor that can be studied. In order to evaluate the optimum L_G for the current study to maximize the wind load reduction, a gap size of 0.5 W_M, W_M, and 1.5 W_M are examined. The simulations are

performed over the deflector-module combination structure under a wind direction of 0°. The results are shown in Table 4.9.

Table 4. 8 C_N, C_L, and C_D over the module with deflector in front under wind direction 0° with different spacing L_G

Gap size L_G	C_N	C_L	C_D
0.5 W_M	1.14	-0.44	1.05
W_M	1.49	-0.58	1.37
1.5 W_M	1.40	-0.54	1.29

Based on the current PV module geometry, the deflector with 0.5 W_M spacing in front of the module has the best performance within these tested gap sizes.

4.5 Different Module Inclination Angle θ

In this section, the role of the flow deflector on changing the wind load on the PV module is examined for different module inclination angles other than 25°. The inclination angle θ is defined in Figure 3.3 in section 3.3.1. As stated in Shademan et al.'s research on wind loading on solar panels at different angles of inclination [48], the wind load on the PV module is expected to increase with the rise of the angle of inclination.

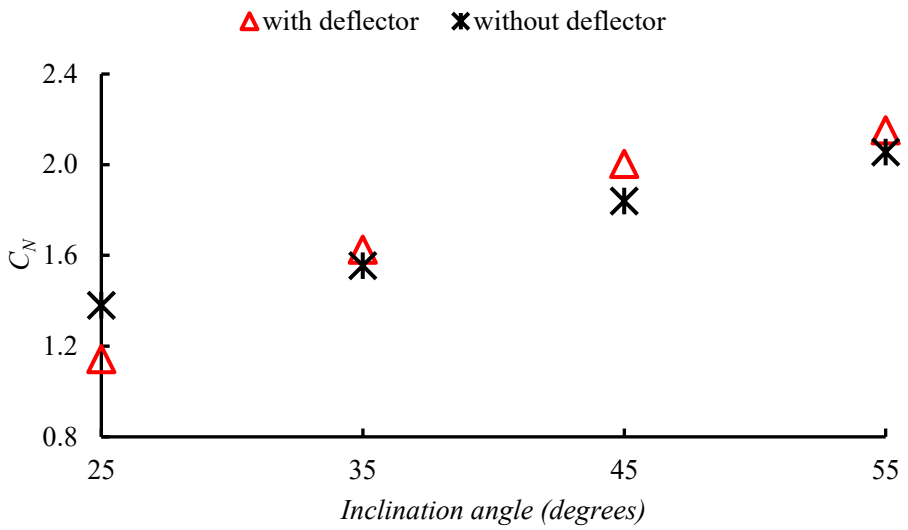

Figure 4. 21 Comparison of the C_N on the PV system with different inclination angles

As shown in Figure 4.21, the wind load on the module rises with an increase in the angle of inclination of the module. However, the tested inclination angles are with a 10° interval, whether the increase of the C_N is linear to the increase of the inclination angle needs further study. The studied deflector geometry results in an effective C_N reduction at an inclination angle of 25°. To identify what leads to the increase of the C_N, the inclination angle of 35° cases is taken as an example to address the flow changes near the module. The velocity and TKE distributions in the domain are presented.

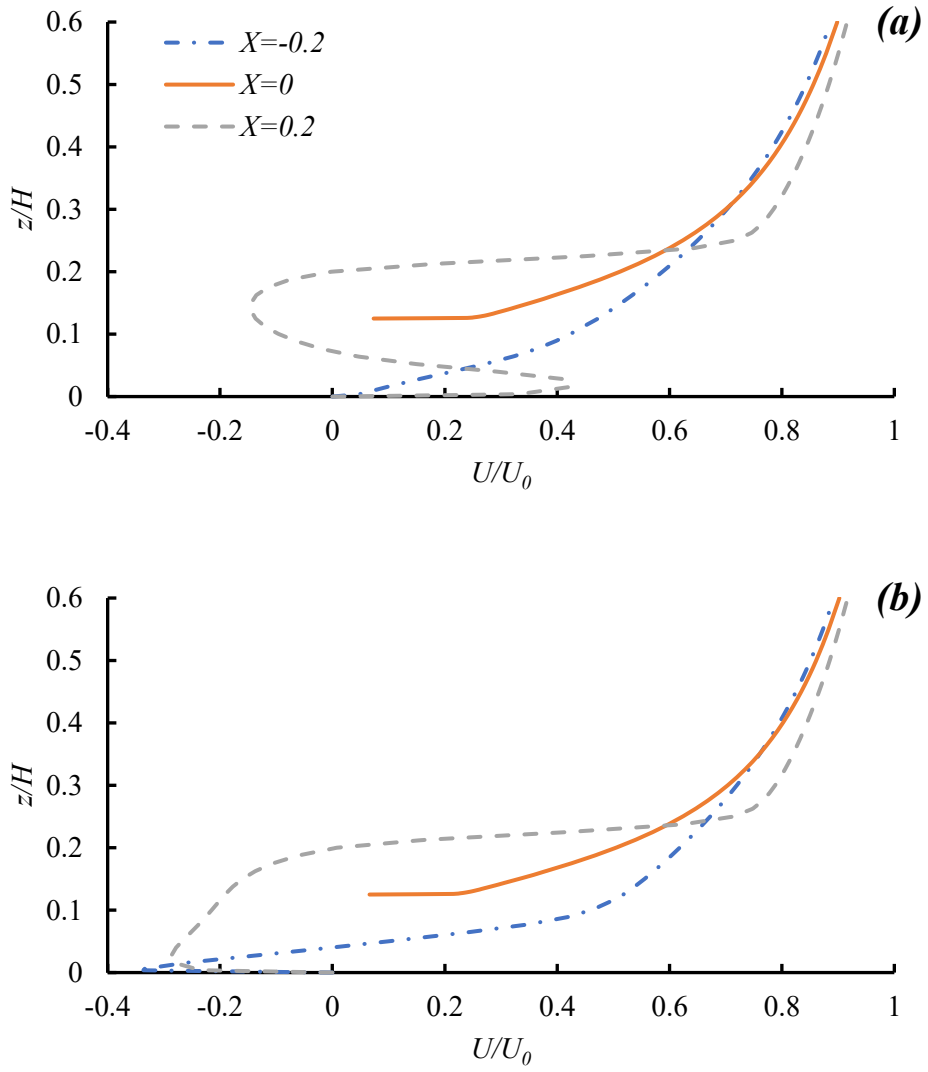

Figure 4. 22 Streamwise velocity distribution near a PV module at the inclination angle of 35° under wind direction 0° (a) without the deflector and (b) with the deflector

The velocity distribution in the *x*-direction close to the module upstream, shown in Figure 4.22, is very similar to the profile shown in Figure 4.8 (a), which is the streamwise velocity distribution near the module at an inclination angle of 25°. The velocity above the

module remains almost unchanged, while it used to increase at an angle of inclination of 25°, which shows that the deflector has no impact on the flow behavior on the windward surface of the module. Downstream of the module ($X = 0.2$), an increase in velocity in the reverse direction is found near the ground compared with the x velocity distribution near the module at an angle of inclination of 25° (shown in Figure 4.9 (a)), which suggests a decrease of the drag near the lower section of the module. While the streamwise velocity distribution shows little change near the upper section of the module ($z/H > 0.1$), the increase of the C_D (from 0.87 to 0.91) is in favor of the module at the 35° inclination angle.

Table 4. 9 C_N on the tested inclined module under wind direction 0° with and without the flow deflector in front of the module

Inclination angle	C_N without deflector	C_N with deflector	C_N change
25°	1.38	1.14	-17.12%
35°	1.56	1.63	+4.55%
45°	1.84	2.00	+8.90%
55°	2.06	2.15	+4.61%

As shown in Table 4.8, the C_N on the module increases by 4.55% after applying the deflector to the 35° inclined module. The increase of the C_N on the module is 8.90% and 4.61% for inclination angles 45° and 55°, respectively. The deflector fails to make an effort

on the flow near the windward surface of the module as significant as the inclination angle of the module is at 25°. In order to achieve similar results of the flow near the 25° inclined PV module after applying the flow deflector in front, either increasing the height of the deflector or shortening the L_G is suggested while the inclination angle of the module is greater than 25°.

4.6 Wind Load Changes Applying the Deflector to the Arrayed Photovoltaic System

For an arrayed photovoltaic modular system, the current study is investigating a column of five panels. The gap size (distance between the closest edges) between the panels is W_M, which is the width of the panel, following the suggested row-gap size by Shademan et al. [8].

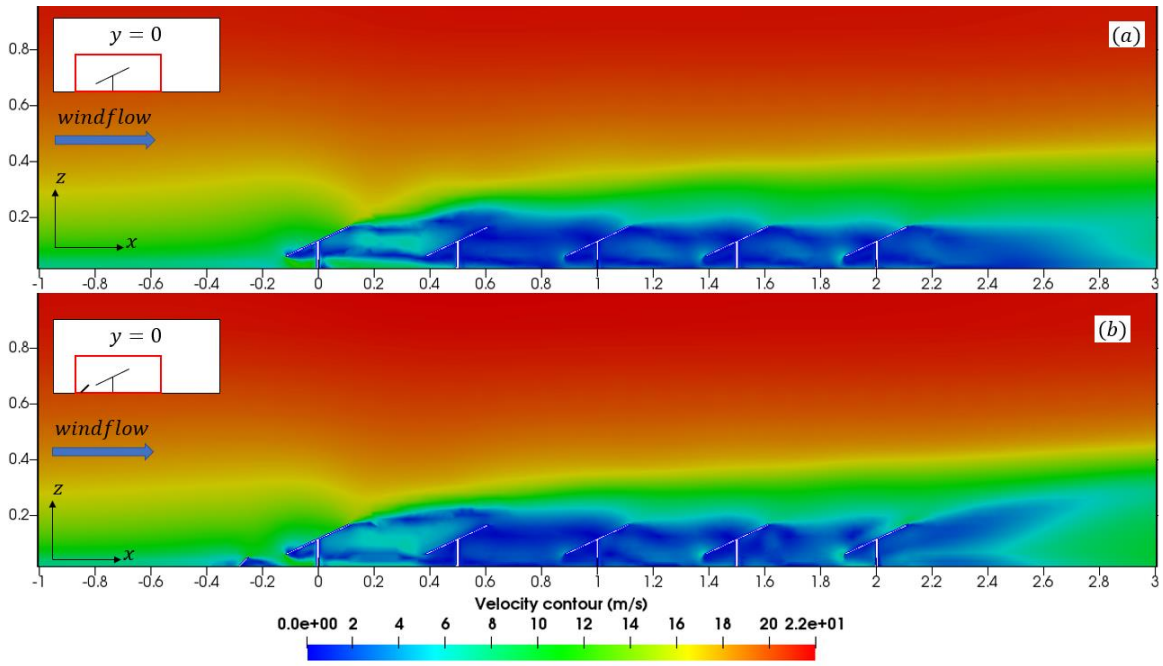

Figure 4. 23 Streamwise velocity distribution near arrayed panels (a) without and (b) with the flow deflector under wind direction 0°

Figure 4.23 illustrates the velocity distribution along *y=0*. The sheltering effect [49] is expected as the first-row module experiences the highest wind load. The module in the second to the fifth row in the array experiences much less wind load than the first row does.

For the first-row module, the presence of the deflector postponed the reattachment point of the recirculation region at the upper surface near the lower edge of the module. Also, the streamwise velocity distribution near the upper section of the leeward surface of the module is increased significantly (from dark blue to light), suggesting a decrease in the drag. The *x* velocity distribution changes shown in Figure 4.23 near the first-row module are similar to the *x* velocity distribution changes near the stand-alone module with the flow deflector shown in Figure 4.6. The changes in the streamwise velocity distribution near the second- to the fifth-row modules are found to be negligible.

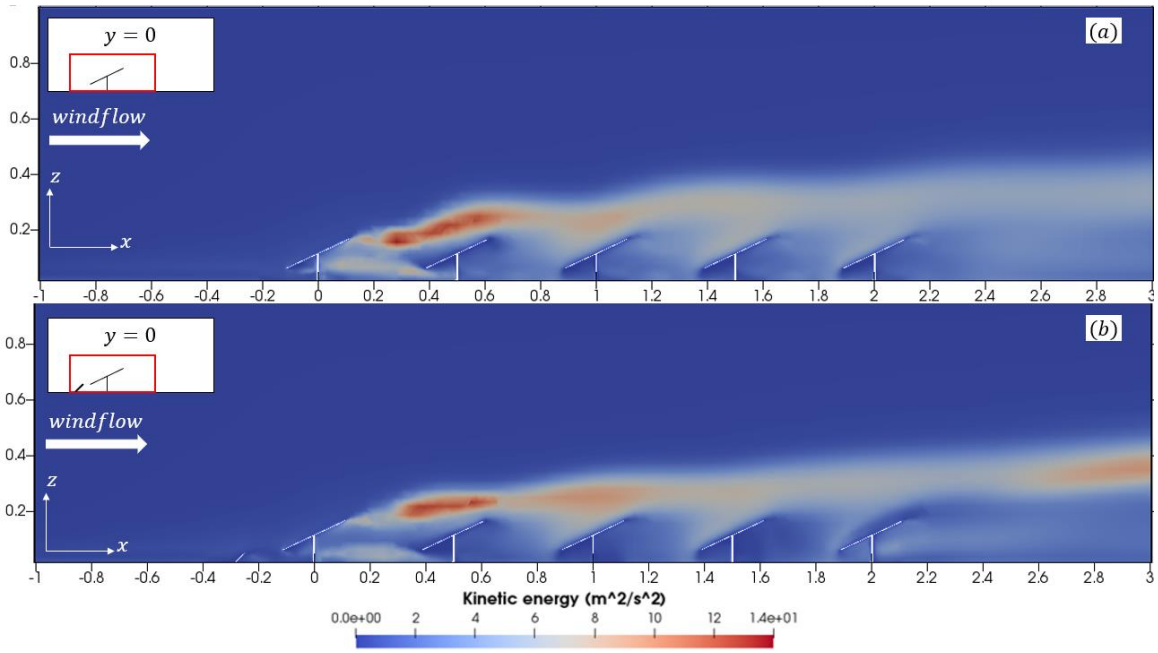

Figure 4. 24 TKE distribution of arrayed panels (a) without and (b) with the deflector at wind direction 0°

The TKE distribution is illustrated in Figure 4.24. The high TKE region between the first- and the second-row modules is shifted higher (farther) from the upper surface of the second-row module with the presence of the flow deflector in front of the first-row module. However, the TKE profile near the surfaces of the modules is barely changed.

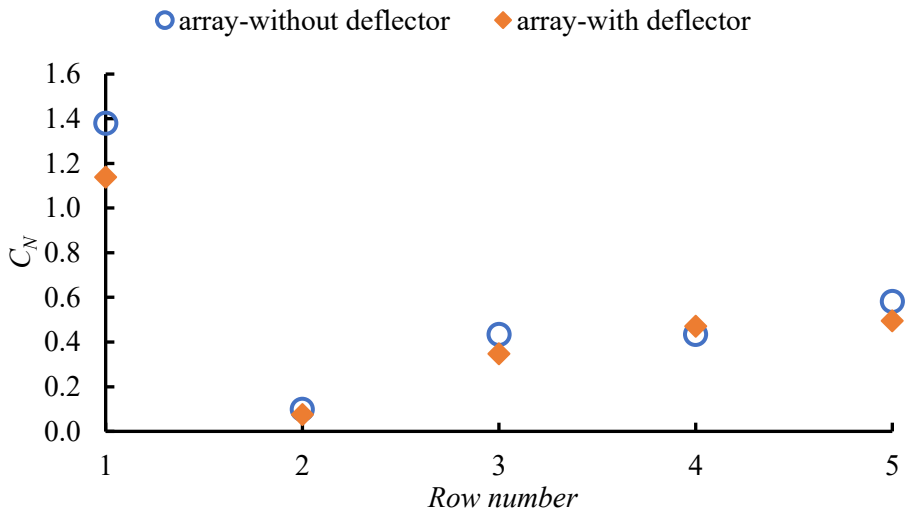

Figure 4. 25 C_N of the module in each row of the array with and without the flow deflector in front

The C_N shown in Figure 4.25 indicates that applying the deflector in front of the single-column array with five rows can effectively reduce the wind load on the most critical module, the first-row one. Both the results in the current study and the wind loading research on the solar array by Shademan et al. [48] indicate that for a single column array,

the first-row module experiences the highest wind load. The presence of the deflector in front of the first-row module contributes to reducing the critical wind load on the first-row module from a C_N value of 1.38 to 1.14, or by 17.39%. For the modules in the second to the fifth rows of the array, the changes in both velocity and TKE profiles near the modules remain low where the C_N changes are less than 10%.

Chapter 5. CONCLUSIONS AND FUTURE WORKS

5.1 Conclusions

This thesis investigated the wind load over a PV system with and without the flow deflector. When the velocity, pressure, and turbulence kinetic energy distribution were compared, combined with the net pressure coefficients changes, the use of the deflector on the ground-mounted PV system showed several significant changes:

(i) Adding the flow deflector reduced the pressure difference between the two sides of the PV module, leading to lower aerodynamic loads on the module. The wind load reduction was significant among almost all the tested wind directions. The wind load reduction on the PV module when the deflector was placed facing the inlet wind flow direction was significant, with a maximum of nearly 40%.

(ii) The existence of the holding structure affected the flow in the wake of the module. Furthermore, when the support structure at the leeward side was considered during the flow study, it could contribute to changes in the recirculation region, which was critical for wind load evaluation on the PV module.

(iii) The current flow deflector geometry (a 45° slope with a 0.5 *m* height in full-scale) could effectively reduce the wind load on the PV module with a 25° inclination angle. The

increase of the wind load under other inclination angles (35° to 55° with 10° interval) showed that, in order to use the flow deflector to reduce the aerodynamic load, the dimension of the deflector needed to be adjusted according to the object PV module dimension.

(iv) The presence of the flow deflector to the PV array is able to reduce the wind load on the module in the first row, which is the module that experiencing the highest wind load in the array.

(v) The idea of the flow deflector is with the advantages of economical friendly, flexibility, and strong environmental adaptability. The potential of the deflector and deflector-like structures are considerable, which all can be used to help the PV systems expansions across the world and avoid being limited by the local environmental conditions.

5.2 Future Works

As the idea of the flow deflector needs to be further investigated before being applied to the fields, three main study directions need to be considered for future researchers.

i. Actual-scale wind tunnel experiments with the corresponding settings.

ii. Investigate the temperature changes near the module surfaces before and after applying the flow deflector, which is associated with the efficiency of the PV system.

iii. Compare results using different turbulence models and methods (including LES) to further address the turbulence structure changes after applying the deflector to the PV module.

APPENDIX A: Equations and Methodology

A 1. Simplified NS equations

Simplified NS equations for incompressible steady flows.

$$div\,\mathbf{u} = 0 \qquad (A1)$$

$$\frac{\partial u}{\partial t} + div(u\mathbf{u}) = -\frac{1}{\rho}\frac{\partial P}{\partial x} + v\,div\big(grad(u)\big) \qquad (A2a)$$

$$\frac{\partial v}{\partial t} + div(v\mathbf{u}) = -\frac{1}{\rho}\frac{\partial P}{\partial y} + v\,div\big(grad(v)\big) \qquad (A2b)$$

$$\frac{\partial w}{\partial t} + div(w\mathbf{u}) = -\frac{1}{\rho}\frac{\partial P}{\partial z} + v\,div\big(grad(w)\big) \qquad (A2c)$$

In the equations, *u, v, w* are the components from velocity vector $\boldsymbol{u}$ according to *x, y, z* components. ρ is the density of the air, *P* is the pressure, *v* is the kinematic viscosity.

A 2. Explanation of the terms in turbulence model $\boldsymbol{k-\varepsilon}$

The terms in equation (3) and (4) in section 3.2.2 are as follows:

$$Rate\ of\ change\ of\ k\ (\varepsilon) + Transport\ of\ k\ (\varepsilon)\ by\ convection =$$

$$Transport\ of\ k\ (\varepsilon)\ by\ diffusion + Rate\ of\ production\ of\ k\ (\varepsilon) - rate\ of\ destruction\ of\ k\ (\varepsilon)$$

APPENDIX B: OpenFOAM Modifications

Since the inlet velocity profile is not following the power law, customization is needed to define the inlet velocity profile. The customized functions or applications were built through the process of compiling. Like all the other default applications, the customized one contains a "*.C" file and a "*.H" file, which are the definition file and the developing the class file. These two files together defined an inlet boundary condition where is needed in the current research. After these two files were built, a compiler was employed to make the current boundary condition be recognized by OpenFOAM. A folder named "Make" is needed inside the application definition folder. The current boundary is defined as the name "benchmark"; it copied the existing similar boundary condition. The old dependency of the condition was removed by OpenFOAM utility "wclean". After the modifications, the new boundary condition was compiled by compiler "wmake" to add it to the OpenFOAM library.

REFERENCE

[1] World Bank, “Fossil fuel energy consumption (% of total) | Data,” *Data, Energy: Fossil fuel consumption*. 2016.

[2] A. Lehner, “Solar PV | Student Energy.” [Online]. Available: https://www.studentenergy.org/topics/solar-pv.

[3] “Renewable energy facts,” *Natural Resources Canada*, 2019. [Online]. Available: https://www.nrcan.gc.ca/science-data/data-analysis/energy-data-analysis/energy-facts/renewable-energy-facts/20069.

[4] “Solar Power World takes a look at the history of solar energy.” [Online]. Available: https://www.solarpowerworldonline.com/2018/01/long-history-solar-pv/.

[5] C. M. Jubayer and H. Hangan, “Numerical simulation of wind effects on a stand-alone ground-mounted Photovoltaic (PV) system,” *J. Wind Eng. Ind. Aerodyn.*, vol. 134, pp. 1–37, 2014.

[6] C. M. Jubayer and H. Hangan, “A numerical approach to the investigation of wind loading on an array of ground-mounted solar photovoltaic (PV) panels,” *J. Wind Eng. Ind. Aerodyn.*, vol. 153, pp. 60–70, 2016.

[7] and V.-E. R. GEORGETA BĂETU*, CARMEN-ELENA TELEMAN, ELENA AXINTE, “Numerical simulation of wind action on a solar panels array for different wind directions,” no. Lxiii, 2013.

[8] M. Shademan, R. M. Barron, R. Balachandar, and H. Hangan, “Numerical simulation of wind loading on ground-mounted solar panels at different flow configurations,” *Can. J. Civ. Eng.*, vol. 41, no. 8, pp. 728–738, 2014.

[9] W. P. Warsido, G. T. Bitsuamlak, J. Barata, and A. Gan, “Influence of spacing parameters on the wind loading of the solar array,” *J. Fluids Struct.*, vol. 48, pp. 295–315, 2014.

[10] A. Abiola-Ogedengbe, H. Hangan, and K. Siddiqui, “Experimental investigation of wind effects on a stand-alone photovoltaic (PV) module,” *Renew. Energy*, vol. 78, pp. 657–665, 2015.

[11] G. P. Reina and G. De Stefano, “Computational evaluation of wind loads on sun-

tracking ground-mounted photovoltaic panel arrays," *J. Wind Eng. Ind. Aerodyn.*, vol. 170, no. August, pp. 283–293, 2017.

[12] M. Mammar, S. Djouimaa, U. Gärtner, and A. Hamidat, "Wind loads on heliostats of various column heights: An experimental study," *Energy*, vol. 143, pp. 867–880, 2018.

[13] H. Irtaza and A. Agarwal, "CFD Simulation of Turbulent Wind Effect on an Array of Ground-Mounted Solar PV Panels," *J. Inst. Eng.*, vol. 99, no. 2, pp. 205–218, 2018.

[14] A. López, V. E. Parnás, and J. Cataldo, "Wind tunnel experiments on ground-mounted photovoltaic solar panels," *Rev. Ing. Constr.*, vol. 34, no. 1, pp. 15–24, 2019.

[15] M. Shademan, R. Balachandar, and R. M. Barron, "Detached eddy simulation of flow past an isolated inclined solar panel," *J. Fluids Struct.*, vol. 50, pp. 217–230, 2014.

[16] A. Abiola-ogedengbe, "Experimental investigation of wind effect on solar panels," 2013.

[17] E. X. Ted Stathopoulos, Ioannis Zisis, "Wind Loads on Solar Collectors: A Review," 2012, pp. 1169–1179.

[18] C. T. Adrian Radu, Elena Axinte, "Steady wind pressures on solar collectors on flat-roofed buildings," *J. Wind Eng. Ind. Aerodyn.*, vol. 23, pp. 249–258, 1986.

[19] H. Ruscheweyh and R. Windhövel, "Wind loads at solar and photovoltaic modules for large plants."

[20] G. A. Kopp, S. Farquhar, and M. J. Morrison, "Aerodynamic mechanisms for wind loads on tilted, roof-mounted, solar arrays," *J. Wind Eng. Ind. Aerodyn.*, vol. 111, pp. 40–52, 2012.

[21] G. A. Kopp, D. Ph, P. Eng, and M. Asce, "Wind Loads on Low-Profile, Tilted, Solar Arrays Placed on Large, Flat, Low-Rise Building Roofs," no. 2013, pp. 1–11, 2014.

[22] M. T. L. Browne, M. P. M. Gibbons, S. Gamble, and J. Galsworthy, "Wind loading on tilted roof-top solar arrays: The parapet effect," *J. Wind Eng. Ind. Aerodyn.*, vol. 123, pp. 202–213, 2013.

[23] A. M. Aly and G. Bitsuamlak, “Wind-Induced Pressures on Solar Panels Mounted on Residential Homes,” no. 2010, pp. 1–13, 2013.

[24] J. Cao, A. Yoshida, P. K. Saha, and Y. Tamura, “Wind loading characteristics of solar arrays mounted on flat roofs,” *J. Wind Eng. Ind. Aerodyn.*, vol. 123, pp. 214–225, 2013.

[25] R. N. Pratt and G. A. Kopp, “Velocity measurements around low-profile, tilted, solar arrays mounted on large flat-roofs, for wall-normal wind directions,” *J. Wind Eng. Ind. Aerodyn.*, vol. 123, pp. 226–238, 2013.

[26] D. Banks, “The role of corner vortices in dictating peak wind loads on tilted flat solar panels mounted on large, flat roofs,” *Jnl. Wind Eng. Ind. Aerodyn.*, vol. 123, pp. 192–201, 2013.

[27] C. Geurts and P. Blackmore, “Wind loads on stand-off photovoltaic systems on pitched roofs,” *Jnl. Wind Eng. Ind. Aerodyn.*, vol. 123, pp. 239–249, 2013.

[28] S. E. Stenabaugh, Y. Iida, G. A. Kopp, and P. Karava, “Wind loads on photovoltaic arrays mounted parallel to sloped roofs on low-rise buildings,” *Jnl. Wind Eng. Ind. Aerodyn.*, vol. 139, pp. 16–26, 2015.

[29] A. Naeiji, F. Raji, and I. Zisis, “Wind loads on residential-scale rooftop photovoltaic panels,” *J. Wind Eng. Ind. Aerodyn.*, vol. 168, no. February, pp. 228–246, 2017.

[30] J. Wang, Q. Yang, and Y. Tamura, “Effects of building parameters on wind loads on flat-roof-mounted solar arrays,” *J. Wind Eng. Ind. Aerodyn.*, vol. 174, no. June 2017, pp. 210–224, 2018.

[31] C. Chu and S. Tsao, “Aerodynamic loading of solar trackers on flat-roofed buildings,” *J. Wind Eng. Ind. Aerodyn.*, vol. 175, no. February, pp. 202–212, 2018.

[32] X. Ortiz, D. Rival, and D. Wood, “Forces and Moments on Flat Plates of Small Aspect Ratio with Application to PV Wind Loads and Small Wind Turbine Blades,” pp. 2438–2453, 2015.

[33] A. Schellenberg, J. Maffei, K. Telleen, and R. Ward, “Structural analysis and application of wind loads to solar arrays,” *J. Wind Eng. Ind. Aerodyn.*, vol. 123, pp. 261–272, 2013.

[34] A. M. Aly, “On the evaluation of wind loads on solar panels: The scale issue,” *Sol.*

Energy, vol. 135, pp. 423–434, 2016.

[35] A. Mousaad and G. Bitsuamlak, “Aerodynamics of ground-mounted solar panels : Test model scale effects,” *Jnl. Wind Eng. Ind. Aerodyn.*, vol. 123, pp. 250–260, 2013.

[36] K. Ã. Chung, K. Chang, and Y. Liu, “Reduction of wind uplift of a solar collector model,” *J. Wind Eng. Ind. Aerodyn.*, vol. 96, pp. 1294–1306, 2008.

[37] K. Chung, K. Chang, and C. Chou, “Wind loads on residential and large-scale solar collector models,” *Jnl. Wind Eng. Ind. Aerodyn.*, vol. 99, no. 1, pp. 59–64, 2011.

[38] K. M. Chung, C. C. Chou, and K. C. Chang, “Blockage effects on surface pressures: The case of an inclined flat plate with and without a guide plate,” *J. Chinese Inst. Eng. Trans. Chinese Inst. Eng. A/Chung-Kuo K. Ch’eng Hsuch K’an*, vol. 37, no. 7, pp. 915–922, 2014.

[39] A. M. P. Ivo Marini c-Kragi c a, Sandro Ni zeti c, Filip Grubi si c- Cabo, “Analysis of flow separation effect in the case of the free-standing photovoltaic panel exposed to various operating conditions,” *J. Clean. Prod.*, vol. 174, pp. 53–64, 2018.

[40] P. K. Saha, A. Yoshida, R. Okada, and Y. Tamura, “Reduction of Mean Wind Forces on Photovoltaic System using Aerodynamic Appendages,” *KSCE J. Civ. Eng.*, vol. 22, no. 9, pp. 3395–3400, 2018.

[41] M. Markousi, D. K. Fytanidis, and J. V Soulis, “Wind Load Reduction in Hollow Panel Arrayed Set,” vol. 2016, 2016.

[42] H. Bendjebbas, A. A. El-hadj, and M. Abbas, “Numerical simulation of the effect of wind barrier openings on high-speed wind flow around a heliostat field,” *Appl. Math. Model.*, vol. 61, pp. 443–456, 2018.

[43] C. Schwingshackl, M. Petitta, J. E. Wagner, and G. Belluardo, “Wind Effect on PV Module Temperature : Analysis of Different Techniques for an Accurate Estimation Wind effect on PV module temperature : Analysis of different techniques for accurate estimation,” *Energy Procedia*, no. April, 2013.

[44] M. Z. Jacobson and V. Jadhav, “World estimates of PV optimal tilt angles and ratios of sunlight incident upon tilted and tracked PV panels relative to horizontal

panels," *Sol. Energy*, vol. 169, no. April, pp. 55–66, 2018.

[45] S. A. Orszag, "Analytical theories of turbulence," *J. Fluid Mech.*, vol. 41, no. 2, pp. 363–386, Apr. 1970.

[46] A. Tarokh, M. A. Mohamed, D. Wood, and C. Johansen, "Turbulence model assessment and scaling results for wind flow over a simulated building," in *Cwe2015*, 2015, pp. 1–8.

[47] H. P. G. Menter F.R., Langtry R., Völker S., "Transition Modelling for General Purpose CFD Codes," *Eng. Turbul. Model. Exp.*, pp. 31–48, 2005.

[48] M. Shademan and H. Hangan, "Wind Loading on Solar Panels at Different Inclination Angles," *11th Am. Conf. Wind Eng.*, 2009.

[49] J. E. Girma T. Bitsuamlak, Agerneh K. Dagnew, "Evaluation of wind loads on solar panel modules using CFD," in *The Fifth International Symposium on Computational Wind Engineering (CWE2010)*, 2010, no. December.